POLITECNICO DI TORINO

Department of Applied Science and Technology
Ph.D. in Chemical Engineering
XXVII Cycle (2012-2014)

AN IN-SILICO OPEN-SOURCE APPROACH FOR THE INVESTIGATION OF MULTI-PHASE PACKED SYSTEMS: RIGID BODY SIMULATIONS AND COMPUTATIONAL FLUID DYNAMICS

PhD Student

Gianluca Boccardo

Supervisors
Prof. Daniele Marchisio
Prof. Rajandrea Sethi

Second Referee:
Dr. Frederic Augier, Ph.D, HDR

Acknowledgments

iv

Contents

Chapter 1

Introduction

Many systems of practical interest can be characterized as porous (or "packed") media, which can be both natural or engineered.

For example, regarding the former category, in recent years the droughts and water scarcity affecting many parts of the developing and developed world brought renewed attention to the problem of water availability and re-emphasized the necessity of studies of water flow in aquifers.

An even greater push in this direction (and connected with the issue of safe drinking water availability) is given by the growing concerns about environmental contamination of said water sources, be it saltwater intrusion, from chemical contaminants coming from industrial waste, biotic (bacteria or viruses) colloids coming from agricultural waste or even radioactive waste. As a direct consequence, new innovative remediation techniques are being developed and put into application, for which the employment of new and more accurate studies of transport phenomena in porous media are needed. An example over all is the use of micro- and nano- sized zerovalent iron particles degrading non-aqueous organic contaminants in aquifers. In this field of particular interest is the investigation of particle transport in the porous medium, and particle deposition in the grains constituting the porous medium.

Another example of a natural system of great interest is that of oil reservoirs: in recent times, due to the falling in extraction rates caused by the natural exhaustion of oil fields, new techniques are being developed and extensively studied such as polymer flooding and alkali-surfactant methods, which collectively go under the umbrella term of **tertiary** or **enhanced oil recovery**. Also in this field the investigation of (mainly non-Newtonian) fluid flow and scalar transport is of paramount importance.

Regarding artifical systems, a great many of the unit operations relevant

to chemical engineering are carried out in packed system. Some example are catalytic or inert packed bed reactors, trickle bed reactors, all filtration processes and chromatographic separation. While most of these systems have been in use and hence studied for some decades now, new and fast-growing technologies are coming to the forefront of industrial and commercial interest, such is the case of fuel cells: also in this case, new studies focusing on transport in porous media are needed.

This brief overview serves as a reminder of the vastitude of this field and ever-growing importance in today's world. In fact, as it is known and as it has been mentioned, porous media have been studied for a long time. Darcy's famous empirical law relating pressure drop and fluid velocity through a packed system dates back to the nineteenth century; its eventual correction for the accounting of non-linearities arising in the inertial range by Forchheimer, and observations by Knudsen about the so-called *slip flow* of rarefied gases in porous media took place at the start of the twentieth; Brinkman's addition of *effective viscosity* term to Darcy's law, the widely successfully employed Ergun's law, amongst other consolidated studies and theories, followed by a few decades. That is not to say, however, that our knowledge of transport, reaction and other phenomena in porous media is complete. As is it evident, the models that are employed in homogeneous media cannot be directly employed in inhomogeneous ones, as the presence of the solid influences these phenomena in a significant way.

Two problems arise when trying to obtain accurate models when dealing with packed systems, and both of them are related to the *spatial scale* of the problem. First, having made the assumption of working at the continuum scale as it will be the case in this dissertation, the smaller relevant scale at which transport or reaction phenomena are to be studied (the "pore-scale"), can still range from a few millimeters down to a few tens of micrometers: this makes direct observation and the preparation of suitable experiments difficult.

Secondly, the characteristic lengths at which this pore-scale has to be investigated almost never matches the spatial scale at which dynamics of the real system or industrial application develops. This difference could be, in some cases, of many orders of magnitude: suffice as examples the aforementioned cases of water remediation or enhanced oil recovery, where the difference between the micrometer sized pore-scale and the kilometers extension of the aquifer or oil fields is unbridgeable.

The first attempts to tackle this problem were to search for models that could have practical applicability, through ignoring the microscopic structure of the medium and deriving relationships valid at the appropriate

macroscopic scale, and which would take into account the small-scale phenomena through "effective" parameters. This is the case of Darcy's law in which permeability is the upscaled parameter which considers pore structure, while the domain of Darcy's law is a new *pseudo-homogeneous* system, where the difference and the boundary definition between the solid and the fluid zone are lost. While this works quite well for certain problems and under certain conditions (in the latter case, if the fluid is Newtonian and velocities in the Stokes regime), issues arise in a large number of other important cases of interest. For example in the case of catalytic reactors, large experimental campaigns are run in order to obtain macroscale mass transfer and dispersion coefficients, however these studies are not at all straightforward, due to the pore structure which characterises these systems. Near-wall channeling effects and other small-scale complexities may arise, having a great impact on the overall fluid flow and transport process, which are not easy to translate into adequate effective macroscale coefficients. This makes the preparation of comprehensive bench-scale experiments difficult, and results in a challenging scale-up of the results obtained at the small-scale to the larger industrial scale of interest. There are many other examples in which classic macroscopic models fails to represent the actual physical reality, such as the onset of instability in variable density flows, the rate of mixing controlled chemical reactions or mixing-induced precipitation phenomena, and asymmetrical long tails in breakthrough curves in some non-standard systems.

The purpose of the work presented in this thesis is then to tackle both the problem of accurately studying fluid flow, scalar and particle transport and deposition in porous media at the **microscopic scale** (or **pore-scale**), and also to work on how the information and insights gained at the pore-scale can be translated into effective models applicable at the **macroscopic scale**. With respect to the first issue, the approach that we have chosen is to perform detailed **computational fluid dynamics** (**CFD**) analyses of these phenomena. With the growing availability of computational power, which has been in a predictably upward trend in the past decades, CFD can now be used to treat even complex systems and phenomena, like the ones explored in this work. This complexity, in the case of heterogenous systems, as it has been made clear earlier, is first and foremost related to the geometrical structure of porous media, whose characteristic lengths and range of variation can be nigh impossible to reliably reproduce with experiments. In fact, the very first issue our work has encountered was the choice of the geometric models on which to perform CFD simulations or more appropriately, their origin. The choice most frequently made, even

when performing computer simulations, is to start from actual experimentally obtained models of the packed system under investigation, such as X-ray micro-computer-tomography (μ-CT) or scanning electron microscopy (SEM) scans, and then in some way digitize these models for the use in the CFD code. Our approach, for reasons which will be made clear momentarily, has been different. In fact, we decided to use artificial models, which means that we employed algorithmic reconstruction methods to simulate on a computer (given a certain grain shape and grain size distribution function) the packing process and thus obtain a precise representation of the chosen system. Specifically, robust and tested **rigid-body interaction codes** were employed, as it will be described in detail in the relevant chapters.

This choice was made for two reasons, the first of which is practical in nature, as it is much easier to treat computer-generated models as basis for CFD simulations than actual reconstructions of experimental data that, while describing very accurately the porous medium, suffer from big problems in the post-processing of that data in order to extract suitable meshes to use in finite-element or finite-volume codes.

The second reason, central to this work, is to offer a proof of concept of the possibility of investigating complex transport phenomena in systems which are themselves very complex in nature from the standpoint of their geometrical structure, only using an **in-silico framework** and thus relying only on computer simulations, and on experiments just for the needed validation and verification of the latter. Moreover, as it will be made clear, great emphasis has been placed on the choice and use of fully free and open-source codes and software, in order to both stress the importance of the widest possible availability of the research instruments employed herein, and also (maybe more importantly) to provide for the reproducibility of the results presented.

The second issue arises when, having extracted precise models at the pore-scale, it becomes necessary to obtain reliable models for use at the macroscale. As it will be detailed in this work, this has been the endpoint of each CFD simulation campaign and subsequent analysis. Also, there was a specific effort to obtain macroscopic models through the upscaling of the relevant differential equations at the pore-scale through a purely theoretical approach, which is **homogenization through asymptotic expansion**. As it will be shown in detail later on, this approach can both, as stated, provide for upscaled equations for use at the macro-scale but also identify regions of applicability for these same equations, and thus making possible the use of hybrid CFD-macroscale models which, while not being contemplated in this dissertation, are a clear next step in the direction towards a

reliable modeling of complex transport phenomena in porous media.

So, as a brief overview and reading guide, this thesis is organized as follows.

Chapter 2 gives a theoretical background with regards first to incompressible fluid flow in saturated porous media, then to particle dispersion and surface particle deposition phenomena. In all these cases, both the micro- and the macro-scale formulations are given and the multiscale problem is stated, which brings to the last section about homogenization theory, which is laid down in the closing of the chapter.

In **Chapter 3** fluid flow, scalar transport and particle transport in a fully three-dimensional porous medium is described by means of CFD simulations, investigating hydrodynamics dispersion and the coherence of the results with the Fickian hypothesis. In this chapter the algorithmic reconstruction method for the creation of the medium models is first used and described.

Chapter 4 deals with fluid flow in a variety of realistic systems describing a wide variety of catalytic bed packings characterized by different size distributions and catalyst shape. More detail is given with regards to the features of the geometry creation—simulation—analysis open-source framework developed in this thesis. This work has been carried out in collaboration with *IFP-Energies Nouvelles*.

Chapter 5 introduces the problem of surface particle deposition, which is again investigated through CFD simulations performed both in realistic systems and in simplified reconstructions of porous media. Results are compared with other existing correlations based on the "perfect sink" deposition model.

Chapter 6 closes this dissertation by changing the approach to the particle deposition problem, which here is studied via a theoretical upscaling method, which is homogenization theory. The microscale formulation is given, and the macroscale "homogenized" result is presented. The work presented in this chapter has been carried out with the assistance of Prof. Daniel Tartakovsky at University of California, San Diego.

Chapter 2

Theoretical Background

In this chapter, the basics regarding fluid flow, scalar transport and particle transport and deposition in porous media will be covered and explained. A great deal of attention will be given to the analysis and modelling of surface reaction and particle deposition processes. As already stated in the introduction, this has a huge impact on the development of macroscale models for catalytic reactors, filtration processes and aquifer remediation processes employing particulate systems. Then, an overview of the computational methods employed in this work will be provided, ranging from the tools employed in the reconstruction of the porous media models used in the fluid dynamics simulations, to the specifics of the computational fluid dynamics (CFD) work performed. In the last section an overview of the theoretical foundation of homogenization theory will be given and its usefulness in the upscaling process of transport phenomena in porous media will be made clear, setting the stage for the results presented in the last chapter of this thesis.

2.1   Single-Phase Flow in Porous Media

As it has been noted in the previous chapter, the length scales involved in the investigation of transport phenomena in porous media at the scale of the pores are very small: most often at the order of hundreds of micrometers. Even at these scales, the continuum hypothesis holds true, and thus these phenomena are governed by the well known continuity and Navier-Stokes equations, which respectively read as follows:

$$\frac{\partial V_i}{\partial x_i} = 0, \tag{2.1}$$

$$\frac{\partial V_i}{\partial t} + V_j \frac{\partial V_i}{\partial x_j} = -\frac{1}{\rho}\frac{\partial p}{\partial x_i} + \nu \frac{\partial^2 V_i}{\partial x_j^2} \ , \tag{2.2}$$

where V_i is the ith component of the fluid velocity, p is the fluid pressure, and ρ and ν are its density and kinematic viscosity, respectively, and the Einstein or index notation has been used.

However, in the vast majority of cases it would be impractical (and frequently outright impossible) to attempt to describe the flow through a porous medium via a formulation of this kind, that is, a micro-scale formulation. As a matter of fact, this would result in the need for a precise knowledge of the microscopic geometric structure of the whole porous medium, which is unattainable in practice.

Consequently, these problems are traditionally approached using continuum macro-scale formulations, where the relevant variables are the result of an averaging operation carried out on the underlying microscopic features. This kind of treatment entails the loss of distinction between the solid and the fluid portions of the domain, and the elementary particle in this formulation becomes a blended fluid-solid zone, characterized only by its porosity. For clarity, this simplification operation and the loss of information which accompanies it could be considered akin to, at a lower scale, the transition between the molecular description of a fluid and the fluid-continuum description (the one governed by Eqs. (2.1) and (2.2)). Performing these operations, on the continuity and Navier-Stokes equations, results respectively in:

$$\frac{\partial U_i}{\partial x_i} = 0 \ , \tag{2.3}$$

and

$$\frac{\partial U_i}{\partial x_i} + \varepsilon U_j \frac{\partial U_i}{\partial x_j} = -\frac{1}{\rho}\frac{\partial P}{\partial x_i} + g_i - \gamma U_i \ , \tag{2.4}$$

where U_i is the Darcyan velocity in the ith direction, P the upscaled (Darcyan) pressure, γ is the friction factor and g_i the gravity acceleration. Also, as it has been noted, the domain to which these equations apply to is not restricted to the fluid volume anymore, but to the whole porous medium volume, hence the appearance of porosity, ε.

2.1.1 Flow at low Reynolds numbers

The earliest approaches to this problem are to be considered in the context of the search for a simple equation dealing with the relationship between pressure drop and superficial velocity, and implicitly made use of the macroscopic description of a continuous fluid-solid domain just presented. Translated in the notation of the previous section, this corresponds to identifying a constitutive equation for the friction factor γ.

Case in point are the experiments by Henry Darcy, which investigated the aquifer and sand filter system employed in the delivery of freshwater to the city of Dijon. From his work resulted the extremely well-known (and still relevant) *Darcy's law* (Darcy, 1856):

$$\frac{\Delta P}{L} = \frac{\mu}{k}\, q\,, \tag{2.5}$$

where ΔP is the integral pressure drop across the porous medium, L is its length and thus characterizes flow in saturated porous media via its permeability, k, and the fluid superficial velocity q, which corresponds to the magnitude of $\mathbf{U}$ (introduced in Eqs. (2.3) and (2.4)) in the main flow direction. These two last parameters are the result of the aforementioned averaging procedure, and it is apparent how the actual velocity of the fluid inside the pores (henceforward, pore-velocity) differs from the superficial velocity q. Since part of the cross-sectional area (with respect to the main fluid direction) is occupied by the solid matrix, fluid flow takes place only in part of it, leading to a porosity-dependent relationship between the two:

$$V = \frac{q}{\varepsilon}\,, \tag{2.6}$$

where again, with V is to be considered the magnitude of $\mathbf{V}$ (introduced in Eqs. (2.1) and (2.2)) in the main flow direction. This law was originally derived by Darcy himself on phenomenological and experimental grounds, and is valid for low fluid velocities. Equivalently, it can be derived from the "first principles" of fluid flow employing simple conceptual models of a porous medium, and working up from micro- to macro-scale. Neglecting the transient and inertial term in Eq. (2.4) and considering a one-dimensional problem, Darcy's law is obtained, with the friction factor assumed to be constant: $\gamma = \mu/\rho k$, resulting in:

$$\frac{\partial P}{\partial x_i} = \frac{\mu}{k} U_i \; , \tag{2.7}$$

which, integrated on a finite domain of length L in the main flow direction results in Eq. (2.5).

A clear overview of these approaches can be found in Bear (1988). Moreover, this procedure has also been accomplished, in a particularly mathematically sound way, using the tools of asymptotic homogenization (Hornung, 1997), univocally upscaling Stokes' law for creeping flow to obtain Darcy's law. This (now classic) result will be presented in the second to last chapter of this work, along with its use as a stepping stone towards the upscaling of a specific case of particle transport and deposition. Equation (2.5), while still being useful in many aquifer systems cases characterized by conditions of low fluid flow, has been found to have an upper range of validity, expressed in terms of superficial velocity q. More appropriately, and by analogy with the usual analysis of the laminar-turbulent flow transition, it can be expressed in terms of the Reynolds number (Bear, 1988),

$$\mathrm{Re} = \frac{q\,D_\mathrm{g}}{\nu} \; , \tag{2.8}$$

where the system's characteristic length (usually taken to be the reactor or pipe diameter in the process industry) is the average grain diameter D_g. Details of the calculation of this average diameter for each case considered will be provided later on: but in most cases it is an equivalent diameter calculated from the specific surface of the grains assuming their spherical shape. As such, in the vast majority of cases, Darcy's law will find an upper range of validity at Re ranging from one to ten (Bear, 1988; Hassanizadeh and Gray, 1987).

2.1.2   Flow at high Reynolds numbers

Beyond this limit, the linear relationship expressed in Eq. (2.5) between superficial velocity and the hydraulic gradient ($\Delta P/L$) ceases to be valid, making Darcy's law unsuitable for describing the non-linearities arising under these conditions (Sethi, 2011).

Instead, a similar macroscopic law can be used to that end, which is the *Forchheimer equation* (Forchheimer, 1901; Tosco et al., 2013):

$$\frac{\Delta P}{L} = \frac{\mu}{k}\, q + \beta \rho q |q| \; , \tag{2.9}$$

where β is the so-called inertial flow parameter and, like k, is independent of fluid properties and only depends on the microstructure of the porous medium. Again in terms of the closure needed for the upscaled Eq. (2.4), this corresponds to assuming $\gamma = \frac{\mu}{k} + \beta \rho |q|$.

Various attempts at an explanation of this phenomenon have been made: the most intuitive of which would be to ascribe this nonlinearity to the onset of turbulence, by immediate analogy with the relationship between head loss and fluid velocity for the flow in pipes, which becomes non-linear right after the transition to the turbulent region corresponding to higher Reynolds numbers. The problem with this approach is that while for the flow in pipes the laminar and turbulent zones are clearly identifiable, the transition in the case of flow in porous media is much smoother, with no clear separation between the two: this can be related to what is known for flow around spheres, where the same behaviour is found. As a side note, this is but one example of the difficulties in the conceptualization of simplified models of porous media: what was just mentioned explains why trying to reduce a packed bed (for example) to a collection of straight tubes would fail. Later on it will be shown that the opposite approach (a collection of submerged objects) wouldn't be satisfactory either, with the most promising results coming from a middle-of-the-road approach. Moreover, and even more importantly, a number of experiments were conducted in the past to identify the critical Reynolds number associated with the transition to the turbulent zone in porous media, and found it to be several orders of magnitude higher than the Re at which the nonlinearities begin to become apparent (Schneebeli, 1955; Dudgeon, 1966). Another explanation, and the accepted one, is for this behaviour to be due to the rising importance of inertial forces at higher velocities, whereas they are negligible (with respect to viscous forces) at Re lower than the aforementioned threshold. The concurrency of these two effects together with the flow separation at high Re (due to inertial forces) in the zones where flow abruptly changes direction in the vicinity of a solid wall, explain the observed relationship between pressure drop and superficial velocity. A more in-depth review of these concepts can be found in Bird et al. (1960); Bear (1988).

Amongst the various conceptual models used in porous media modeling, one that has been particularly successful is a modified form of the mentioned "bundle of tubes" mentioned earlier, which deserves special attention here as

its end results will be the basis for the analyses of fluid flow results performed in this work. An even more in-depth description, along with a comparison with other models (as the somewhat less successful "collection of spheres " model), can be found in Bird et al. (1960). Its origin lies in the attempt to conceptualize and simplify a very important and widely used system in process engineering, which is the packed column. It does so by visualizing it as tangled assembly of crooked tubes, and re-obtaining an appropriate friction factor (starting from the usual expression for smooth tubes) for flow through the entire packed bed. Then, the result is adapted to the cases of both laminar and high-turbulent flow, resulting in the *Blake-Kozeny* and *Burke-Plummer* equations, which read respectively as follows:

$$\frac{\Delta P}{L} = 150 \left(\frac{\mu q}{D_g} \right) \frac{(1-\varepsilon)^2}{\varepsilon^3} \,, \tag{2.10}$$

$$\frac{\Delta P}{L} = \frac{7}{4} \left(\frac{\rho q^2}{D_g} \right) \frac{(1-\varepsilon)^2}{\varepsilon^3} \,. \tag{2.11}$$

These two, after taking care of superposing the expressions to deal with the transition region between laminar and turbulent regimes, can be combined together into the well-known *Ergun's law* (Bird et al., 1960):

$$\frac{\Delta P \rho}{G_0^2} \frac{d_g}{L} \frac{\varepsilon^3}{(1-\varepsilon^3)} = 150 \frac{1-\varepsilon}{(D_g G_0)/\mu} + 1.75 \,, \tag{2.12}$$

where G_0 is the mass flux ($G_0 = \rho \, q$). The Ergun law is often expressed in terms of the dimensionless pressure drop, ΔP^*, and the modified Reynolds number, Re^*, as follows:

$$\Delta P^* = \frac{150}{\mathrm{Re}^*} + 1.75 \,, \tag{2.13}$$

where of course $\Delta P^* = \Delta P \rho d_g \varepsilon^3 / L G_0^2 (1-\varepsilon^3)$ and $\mathrm{Re}^* = D_g G_0 / (1-\varepsilon)\mu$. It has to be noted that this modified Reynolds number differs from the above defined Reynolds number just for the presence of the porosity.

2.2 Scalar/particle transport and deposition/reaction

The same continuum approach used to describe fluid flow at the pore-scale (expressed by Eqs.(2.1), (2.2)) can be adopted to describe scalar transport

and reaction and particle transport and deposition. [1] This results, in an Eulerian framework, in the well-known advection-diffusion equation:

$$\frac{\partial c}{\partial t} + V_j \frac{\partial c}{\partial x_j} = \frac{\partial}{\partial x_j} \left(\mathcal{D} \frac{\partial c}{\partial x_j} \right) \; , \tag{2.14}$$

where c is the pore-scale particle/scalar concentration and $\mathcal{D}$ is the particle/scalar diffusion coefficient. In the case of a reacting scalar this is the standard molecular diffusion coefficient, whereas in the case of particles this is the diffusion coefficient due to Brownian motion, which is in turn generally estimated with the Einstein equation (Einstein, 1905):

$$\mathcal{D} = \frac{k_\mathrm{B} T}{3\pi \mu d_\mathrm{p}} \; , \tag{2.15}$$

where k_B is the Boltzmann constant, T is the temperature, $\mu = \rho \nu$ is the dynamic viscosity of the fluid and d_p is the particle size. The overall approach is valid only if the size of the particles being transported is much smaller than the size of the pores, and if their concentration is low enough to describe diffusive flux through Fick's law. Surface chemical reaction and particle deposition do not usually appear in Eq. (2.14), since they are treated as superficial phenomena. Particle deposition is generally accounted for with a boundary condition at the pore wall. This aspect will be clarified in the later chapters. Beneath a treatment of this kind is the underlying assumption that the solid particles are following the fluid flow along its streamlines: this condition is typically verified for solid particles (of density of about 5000-10000 kg m^{-3}) moving in water at room temperature with size equal to or smaller than 1 μm or, more properly, when the suspended particles' Stokes number, identifying the ratio between the characteristic relaxation time of the particle and that of the fluid is very small ($\ll 1$), as it is the case in the majority of the operating conditions under scrutiny in this work. Following the same steps taken when dealing with fluid flow, a macroscopic equivalent of Eq. (2.14) is usually employed, resulting in:

---

[1]In this work particle and scalar transport are treated with the same approach. In fact, when particles are small enough to closely follow the fluid, they can be treated as scalars, advected with the fluid velocity. In this context particle deposition on the surface of the grains constituting the walls of the porous medium can be thought of as a surface chemical reaction involving the transported scalar. Therefore results obtained for particle deposition can be easily employed for simulating scalar transport and reaction.

$$\frac{\partial C}{\partial t} + U_j \frac{\partial C}{\partial x_j} = \frac{\partial}{\partial x_j}\left(\mathbf{D}\frac{\partial C}{\partial x_j}\right) - k_{\mathrm{d}}C \ , \tag{2.16}$$

where U_j is the superficial velocity in the jth direction, C is the macroscale particle concentration, $\mathbf{D}$ is the dispersion tensor whereas k_{d} is the particle deposition rate constant. As already mentioned, the discussion related to Eq. (2.16), which mainly pertains particle deposition, can be easily extended to the problem of transport of a scalar involved in a surface chemical reaction.

2.2.1   Particle dispersion

The dispersion tensor, $\mathbf{D}$, is comprised of two contributes, and is customarily expressed as the sum of the effective (macroscopic) molecular diffusion D_0 and mechanical dispersion (Di Molfetta and Sethi, 2012). The first one (D_0) is the upscaled effect of the molecular diffusion and it is worth noting that while $\mathcal{D}$ is a scalar, its macroscopic counterpart, D_0, could be a tensor when the porous medium is not perfectly isotropic: this is due to the effect of tortuosity (τ or a tensor $\boldsymbol{\tau}$) which slows down particle migration. Mechanical dispersion is instead due to pore structure (and hence fluid streamline) heterogeneities at the pore scale, which result in non uniform distributions of fluid velocities in a pore throat, different velocities among the various pore throats, and in a rise of a transversal component of the velocity, again due to tortuosity. Extensive lab testing has found that the magnitude of mechanical dispersion is proportional to the fluid superficial velocity (Di Molfetta and Sethi, 2012). It is also usually subdivided in two separate contributions identified by two other dispersion coefficients, one representing longitudinal, D_{L}, and the other transversal dispersion, D_{T}. These coefficients (or in general $\mathbf{D}$) depend on the porosity, ε and on the tortuosity of the porous medium and on the Péclet number of the flow $\mathrm{Pe} = qD_{\mathrm{g}}/\mathcal{D}$. Since they can be The effect of diffusion and mechanical dispersion combined is also called hydrodynamic dispersion. Fluid flow both in natural and in engineered systems usually has one main direction (and that is the case in all the systems studied in this work), hence its macroscopic average velocity in that direction can be expressed with a surface averaging operation over the two other (orthogonal) directions of the pore-scale velocity $V_i(\mathbf{x})$, resulting in a one-dimensional form of the velocity $U_x(x)$. The same operation can be performed on pore-scale concentration, resulting in the macroscopic concentration $C(x)$. With these definitions it is straightforward to obtain a

one-dimensional form of Eq. (2.16),

$$\frac{(\partial C \varepsilon)}{\partial t} + U_x \frac{\partial C}{\partial x} = \frac{\partial}{\partial x}\left(\varepsilon D \frac{\partial C}{\partial x}\right) \ , \tag{2.17}$$

where D is a simplified form of the tensor $\mathbf{D}$ of Eq. (2.16), and is a scalar equal to the sum of the effective (as in, macroscale) molecular and longitudinal dispersion coefficients. The difference lies in neglecting flow in the two other orthogonal directions, which causes the transversal dispersion coefficient to be equal to zero and thus the mechanical dispersion to develop only in the longitudinal direction:

$$\left(\epsilon D_0 \frac{\partial C}{\partial x} - \epsilon \langle V_x' c' \rangle\right) = \varepsilon D \frac{\partial C}{\partial x}, \qquad \text{with} \quad D = D_0 + D_{\mathrm{L}}, \tag{2.18}$$

where V_x' and c' are respectively the pore-scale deviations of velocity and concentration from their average values: $V_x' = V_x - U_x/\varepsilon$ and $c' = c - C$. For the unclosed term $\langle V_x' c' \rangle$ an expression akin to the standard Fick's law was implicitly used:

$$\langle V_x' c' \rangle = \frac{1}{\varepsilon \mathcal{L}_y \mathcal{L}_z} \int_0^{\mathcal{L}_y} \int_0^{\mathcal{L}_z} V_x' c' \, \mathrm{d}y \, \mathrm{d}z \approx -D_{\mathrm{L}} \frac{\partial C}{\partial x}. \tag{2.19}$$

When the porosity ε is constant in time, it is possible to rewrite (2.17) as follows:

$$\frac{\partial C}{\partial t} + \left(\frac{U_x}{\varepsilon} - \frac{1}{\varepsilon}\frac{\partial \varepsilon D}{\partial x}\right)\frac{\partial C}{\partial x} = D \frac{\partial^2 C}{\partial x^2} \ , \tag{2.20}$$

The coefficient D, being comprised of two terms respectively accounting for diffusive and advective phenomena, is best described as a function of the Péclet number. For Pe tending to zero, when diffusion predominates, this relationship holds (Bear, 1988):

$$\frac{D}{\mathcal{D}} = \frac{1}{\tau^2} \ , \tag{2.21}$$

Regarding the calculations of τ, many definitions and formulas have been proposed and recent works (Koponen et al., 1996; Clennell, 1997; Duda et al., 2011) have demonstrated their effectiveness and the difference between formulations. The most common definition involves the computations of streaklines (i.e. Lagrangian trajectories) of the flow and the calculation of

the ratio between their length and the porous medium size. Koponen et al. (1996) and Duda et al. (2011) proposed a simpler way to compute τ as a volume integral

$$\tau = \frac{\int |\mathbf{V}|\ d\mathbf{x}}{\int V_\mathrm{x}\ d\mathbf{x}}\ . \tag{2.22}$$

Going to higher Pe numbers other correlations are used. For example a very common one, $D = \alpha U_x$, links the dispersion coefficient to a parameter, α, of the order of the mean grain size. One which is valid for different ranges of Pe (van Milligen and Bons, 2012), is:

$$D \approx \begin{cases} \gamma \mathcal{D} & \text{when}\quad \mathrm{Pe} \ll \delta\sqrt{\mathrm{Pe}_c} \\ \beta \mathrm{Pe}^2/\mathrm{Pe}_c & \text{when}\quad \delta\sqrt{\mathrm{Pe}_c} \ll \mathrm{Pe} \ll \mathrm{Pe}_c \\ \beta \mathrm{Pe} & \text{when}\quad \mathrm{Pe} \gg \mathrm{Pe}_c. \end{cases} \tag{2.23}$$

where γ is the coefficient that scales the macroscale dispersion, D, to the molecular diffusivity, $\mathcal{D}$, for $\mathrm{Pe} \ll 1$ whereas β is the linear coefficient between D, $\mathcal{D}$ and Pe for $\mathrm{Pe} \gg 1$.

This simple relationship is not universally valid, in fact, it typically does not hold for more complex porous media (where, for example, a non-linear relation can appear for high Péclet number) and in the pre-asymptotic regime. Another common expression is the correlation proposed by Bear (1988):

$$\frac{D}{\mathcal{D}} = \gamma + \frac{\alpha V}{\mathcal{D}}\frac{\mathrm{Pe}}{\mathrm{Pe} + 2 + 4\delta^2}, \tag{2.24}$$

where γ and δ have the same physical meaning of the coefficients appearing in Eq. (2.23).

2.2.2   Particle deposition

As far as particles are concerned, the deposition or "collection" performance of a porous medium are usually expressed (Yao et al., 1971; Logan et al., 1995; Tufenkji and Elimelech, 2004) through the deposition rate constant k_d. Once again it is useful to remind here that the results obtained in this context can be extended to the problem of scalars involved in surface reactions. The theoretical concepts can therefore be applied not only to the problem of particle deposition in aquifers and of particle filtration, but also to, for example, reactions in catalytic packed bed reactors. However, for

the sake of clarity, in the following only reference to the particle deposition problem will be made.

It is usually assumed that the deposition rate coefficient is linearly dependent upon particle concentration resulting in the following expression:

$$k_{\mathrm{d}} = \frac{3}{2} \frac{q}{D_{\mathrm{g}}} \frac{1-\varepsilon}{\varepsilon} \alpha \eta_0 \ , \tag{2.25}$$

where η_0 is the collection efficiency and α the attachment efficiency. This latter parameter, depending on the balance between repulsive and attractive forces between colloidal particles and the solid grains can assume values $0 \leq \alpha \leq 1$. In the case of favourable chemical conditions this factor is assumed equal to unity, neglecting the effects of any energy barrier to particle attachment. It has to be noted, though, that hydrodynamic interactions, namely the increase in viscous drag force on the particles in the vicinity of the collector, are also present. As a result, particles' velocity decreases due to the additional friction between the fluid and the wall; this is true even if the particles' Stokes number (as it has been noted being the case in this work) is much lower than unity. This hydrodynamic retardation phenomenon may cause a deviation of some significance in the particles' path from the streamlines of the undisturbed flow near the collector when the distance between the particle and the collector is of the order of two or three particle radii (Goren and O'Neill, 1971). Moreover, the particles' mobility near the wall is also reduced, decreasing the particle diffusivity coefficient which is not constant anymore but depends on the distance to the wall. Corrective factors for both particle velocity and their diffusivity coefficient, accounting for these hydrodynamic interactions, have been obtained in a number of earlier studies (Goren and O'Neill, 1971; Brenner, 1961; Adamczyk et al., 1983).

In this work we will be considering the case where chemical conditions to particle attachment are favourable (as will be explained later on), thus accounting for the contribution of all attractive and repulsive forces (e.g.: London attraction forces) in a single attachment efficiency parameter. In this framework, it wouldn't be possible to include explicitly the effects of hydrodynamic interaction separate from the calculation of these forces as, in the absence of any attractive force, the particles wouldn't be able to reach the collector lacking the means to overcome the viscous repulsion (Rajagopalan and Tien, 1976). A useful approximation in this case is the Smoluchowski-Levich approximation, in which it is assumed that the hydrodynamic retardation experienced by the particle while approaching a solid wall is balanced by the attractive London forces (Levich, 1962; Adamczyk et al., 1983). In

fact, Van der Waals, electrical double layer and hydrodynamic interactions are excluded from the calculations. Neglecting the effects of the latter makes it possible to assume that the particles move with velocity equal to the fluid (as seen earlier) and that the diffusion coefficient is independent of the particle's position in the domain. This approximation is only valid when the particle size is smaller than the thickness of the particle diffusion boundary layer, which sets an upper limit equal to, in the majority of cases, a few hundred nanometres of size (Prieve and Ruckenstein, 1974; Elimelech et al., 1995). This range covers a large part of the cases explored in this work, and an assessment of the possible deviations due to the use of this approximation in the results section of the appropriate chapter.

Particle deposition efficiency

The collection efficiency, η_0, of a single spherical collector is defined as the ratio between the rate of collision of particles with the collector and the rate of particles flowing towards it (Yao et al., 1971)

$$\eta_0 = \frac{\text{rate of particles colliding the collector}}{qC_0 \left(\dfrac{\pi D_{\mathrm{g}}^2}{4} \right)} \ , \tag{2.26}$$

where C_0 is the concentration of particles at a long distance upstream the collector.

The particle deposition rate coefficient in Eq. (2.25), k_{d}, contains the deposition efficiency, η_0, a parameter accounting for all the non-idealities in the transport of particles to the collector and the correlations for its calculation typically include three mechanisms: Brownian diffusion, interception and sedimentation. Interception is a steric effect occurring when particles moving with the fluid along a streamline come into contact with the solid grains due to their finite size, and as such is the endpoint for all deposition mechanisms. Interception of the smallest particles is enhanced by Brownian diffusion, which is the dominant effect for nanoparticles. Interception of the largest particles is enhanced by sedimentation, which acts when their density is higher than that of the carrier fluid and will not be considered in this preliminary work.

There are a number of theoretical models which provide with the means to determine the single collector efficiencies pertaining to each of the transport mechanisms individually, namely Brownian motion, η_{B}, interception, η_{I}, and sedimentation, η_{G}. Precise analytical solutions are thus obtained, which are nonetheless valid only in the simplified system these models were

built on, which is, a single spherical collector immersed in an infinite fluid field in creeping motion.

The simplest case, pertaining Brownian diffusion, was developed by Levich (1962) and builds upon the aforementioned Smoluchowski-Levich approximation, resulting in:

$$\eta_{\mathrm{B}} = 4.04 \mathrm{Pe}^{-\frac{2}{3}} , \tag{2.27}$$

Later, Yao added the case for interception and sedimentation (Yao, 1968), resulting in:

$$\eta_{\mathrm{I}} = \frac{3}{2} N_{\mathrm{R}}^2 , \tag{2.28}$$

and:

$$\eta_{\mathrm{G}} = \frac{(\rho_{\mathrm{p}} - \rho) g d_{\mathrm{p}}^2}{18 \mu q} , \tag{2.29}$$

where N_{R} is the ratio $d_{\mathrm{p}}/D_{\mathrm{g}}$ and ρ_{p} is the solid particles density.

Subsequently then, many works improved on these relations (with regards to Brownian deposition and interception), mainly to account for the influence of the other collectors in the system on the velocity field. For example, taking the steps from the analysis made by Kuwabara (1959), Konstandopoulos et al. (2000) derived the following equations for the single (spherical) collector efficiency:

$$\eta_{\mathrm{B}} = 3.5 \, g(\varepsilon) \mathrm{Pe}^{-\frac{2}{3}} \tag{2.30}$$

and:

$$\eta_{\mathrm{I}} = \frac{3}{2} \frac{N_{\mathrm{R}}^2}{(1 + N_{\mathrm{R}})^s} \, g(\varepsilon)^3 , \tag{2.31}$$

where the exponent $s = (3 - 2\varepsilon)/3\varepsilon$ and $g(\varepsilon)$ is the Kuwabara porosity function:

$$g(\varepsilon) = \left(\frac{\varepsilon}{2 - \varepsilon - \frac{9}{5}(1 - \varepsilon)^{\frac{1}{3}} - \frac{1}{5}(1 - \varepsilon)^2} \right) . \tag{2.32}$$

Another approach (Pfeffer, 1964), and the one more used in recent works,

builds upon the Happel model (Happel, 1958) following the Levich proce-
dure. This model takes accounts for the presence of the other collectors by
considering a shell of fluid around the single spherical collector of the appro-
priate size for the porosity of this unit cell to be equal to that of the whole
bed. In this way, the following result is obtained for the diffusive efficiency:

$$\eta_{\mathrm{B}} = 4As^{\frac{1}{3}}\mathrm{Pe}^{-\frac{2}{3}} \ , \tag{2.33}$$

where As, like $g(\varepsilon)$, is a function of bed porosity:

$$As = \frac{2(1-\gamma^5)}{2 - 3\gamma + 3\gamma^5 - 2\gamma^6} \ , \tag{2.34}$$

where $\gamma = (1-\varepsilon)^{\frac{1}{3}}$. A similar law for interception, which improves Yao's
result, also exists (Elimelech et al., 1995):

$$\eta_{\mathrm{I}} = \frac{3}{2}AsN_{\mathrm{R}}^2 \ . \tag{2.35}$$

From these, it is possible to obtain the total efficiency of the single
spherical collector with the relation (Pfeffer, 1964):

$$\eta_0 = \eta_{\mathrm{B}} + \eta_{\mathrm{I}} + \eta_{\mathrm{G}} \ . \tag{2.36}$$

2.3   Asymptotic homogenization

A mentioned earlier in this chapter, one of the greatest difficulties in the
study of transport phenomena in porous media is the inherent multiscale
nature of the vast majority of processes of interest. A precise model or sim-
ulation describing the local, pore-scale, phenomena would be needed but of
little practical applicability. Hence the need for an upscaled model, equiv-
alent to the first one but able to treat the problem at the macro-scale (in
the case of porous media, the difference spatial scales between the two can
be of many orders of magnitude). A variety of methods are usually em-
ployed to perform this upscaling procedure. One is the method of spatial
averaging, in which a spatial smoothing of the equations valid for a single
phase (the fluid one) is performed in order to obtain equations valid for the
resulting macro-scale pseudo-homogeneous phase, where the details of the
pore structure are lost but the resulting problem can be approached with
classical methods. When performing an averaging operation, the first step is
to identify an appropriate representative elementary volume (REV). Thus,

considering a function u (for example, the pressure of the fluid in the porous medium), the smoothed function will be the results of a local averaging:

$$\langle u \rangle (\mathbf{x}) = \int_{V(\mathbf{x})} u(\mathbf{y}) \mathrm{d}\mathbf{y} \ , \qquad (2.37)$$

where $V(\mathbf{x})$ represents the minimum volume necessary to smooth our the oscillations of function u at the pore scale, resulting in an averaged $\langle u \rangle$ applicable for the treatment of the problem at the macro-scale. A comprehensive reference about this method is found in Whitaker (1999), along with some examples of applications.

Another way of performing this upscaling procedure, and the one used in this thesis work, is the method of asymptotic homogenization (Hornung, 1997). This method is, in general, used to study partial differential equations with rapidly varying coefficients: the usefulness in treating porous media, which possess rapidly changing structure at the microscale, is then obvious.

In this case, the emphasis is not placed on the identification of a representative volume, but instead on considering a family of functions u^ξ, where ξ is a length scale parameter identifying the ratio of the period of the structure (or of the oscillation of the coefficients of the differential equation) to the macroscopic length scale of the problem. This results in a hierarchy of problems parameterized by the scale parameter ξ, with the end point of the procedure being the determination of the limit

$$u = \lim_{\xi \to 0} u^\xi \ , \qquad (2.38)$$

where u is the resulting upscaled equation, as $\langle u \rangle$ was in the case of spatial averaging. In short, the core of the distinction between the two methods is that the former comes to the macroscale form of the equations by smoothing and spatial averaging, while with homogenization the upscaled equation is obtained by letting the microscale (described by the parameter ξ) tend to zero, as is shown in Fig. 2.1.

2.3.1 Multiple-scale expansion in periodic media

A number of different methods exist to treat the problem of solving the limit in Eq. (2.38) and obtaining the effective coefficients for the macroscale equation: among these are the *multiple-scale* method, the *energy* method (or more appropriately the *oscillating test functions* method), the *probabilistic*
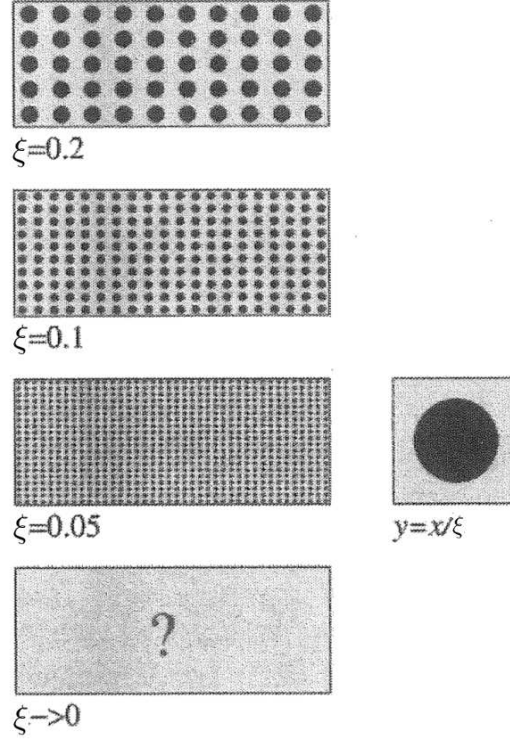
Figure 2.1: Homogenization of the porous medium as the limit of ξ tends to zero. Image from Hornung (1997).

formulation and the *spectral decomposition of operators* (the so-called expansion in Bloch waves). In this work the multiple-scale method will be used, of which a brief description will be now given. For a more in-depth discussion of both this method and the others mentioned, excellent explanations can be found in the foundational works of Palencia (1980), Bensoussan et al. (1980), Cioranescu and Donato (2000) and especially in Hornung (1997).

Let Ω be a bounded open set in $\mathbb{R}^N$ with a smooth boundary $\mathrm{d}\Omega$, $\xi > 0$ the aforementioned scale parameter (with value tending to zero). We can consider the general equation

$$\mathcal{A}_\xi u^\xi = f \ , \tag{2.39}$$

with a Dirichlet boundary condition for u on $\mathrm{d}\Omega$. This model case is relevant both for the laying out of homogenization theory (as most of the theoretical hurdles to solve are already present in this case) and for a lot of practical applications. The expression $\mathcal{A}_\xi$ is a compact way of describing a

family of partial differential operators

$$\mathcal{A}_\xi = - \sum_{i,j=1}^{N} \frac{\partial}{\partial x_i} \left(a_{ij}^\xi \frac{\partial}{\partial x_j} \right) , \qquad (2.40)$$

A classic form of this problem is the diffusion case

$$\begin{cases} -\nabla \cdot (a^\xi(\mathbf{x}) \nabla u^\xi(\mathbf{x})) = f & x \in \Omega \\ u(\mathbf{x}) = u_{\mathrm{D}}(\mathbf{x}) & x \in \partial\Omega \end{cases} \qquad (2.41)$$

where the coefficient a^ξ is rapidly oscillating, which means that it can be expressed as

$$a^\xi(\mathbf{x}) = a \left(\frac{\mathbf{x}}{\xi} \right) , \qquad (2.42)$$

for all $\mathbf{x} \in \Omega$. Moreover, the function a is Y-periodic in $\mathbb{R}^N$ with periodicity cell $Y = \{\mathbf{y} = (y_1, \ldots, y_N) : 0 < y_i < 1 \text{ for } i = 1, \ldots, N\}$.

Here lies one of the core assumptions of homogenization theory, which is the existence of two separate scales for the phenomenon under investigation, described by two different separate variables. The macroscale, for which Eq. (2.41) is written, is described by the "slow" variable $\mathbf{x}$, while the microscale, where the rapid changes in the pore structure (or, in the sense of the model problem of Eq. (2.41), the coefficients a_i) happen, is described by the "fast" variable $\mathbf{y} = \dfrac{\mathbf{x}}{\xi}$. In short, $\mathbf{x}$ gives the position of a point in the domain Ω where $\mathbf{y}$ gives the position in the reference cell Y. Figures 2.2 and 2.3 exemplify this concept (albeit referring to the case of a periodic medium with obstacles, which shall be introduced momentarily). Implicitly, an assumption is also made about the existence of a periodically repeating cell constituting the porous medium. In many cases this could be untrue, but this simplifying assumption is not a limitation as it can be shown that both periodic and randomly arranged media can be treated in this way resulting in a similar macroscopic description (see Auriault and Adler (1995) and Auriault (1991) for more details). Framing the problem in this two-scale interpretation brings about the *ansatz* stating the existence of a formal asymptotic expansion for u^ξ of the form

$$u^\xi(\mathbf{x}) = u_0(\mathbf{x}, \mathbf{y}) + \xi u_1(\mathbf{x}, \mathbf{y}) + \xi^2 u_2(\mathbf{x}, \mathbf{y}) + \ldots , \qquad (2.43)$$

where the coefficient functions u_j for $j = 1, 2, \ldots$ are defined for $\mathbf{x} \in \Omega$ and $\mathbf{y} \in Y$ and are Y-periodic. Now, regarding the differential operators

$\mathcal{A}_\xi$, consider a generic function $\Psi = \Psi(\mathbf{x}, \mathbf{y})$ depending on two variables in $\mathbb{R}^N$ and express as Ψ_ξ the following:

$$\Psi_\xi(\mathbf{x}) = \Psi(\mathbf{x}, \mathbf{y}) = \Psi(\mathbf{x}, \frac{\mathbf{x}}{\xi}) \ . \tag{2.44}$$

Notice that the derivatives obey the law

$$\frac{\partial \Psi_\xi}{\partial x_i}(\mathbf{x}) = \frac{\partial \Psi}{\partial x_i}(\mathbf{x}, \mathbf{y}) + \frac{1}{\xi}\frac{\partial \Psi}{\partial y_i}(\mathbf{x}, \mathbf{y}) \tag{2.45}$$

in index notation, or or more compactly with differential operators:

$$\nabla = \nabla_x + \frac{1}{\xi}\nabla_y \ . \tag{2.46}$$

Consequently, using Eq. (2.43) and Eq. (2.46) in Eq. (2.41), it is immediate to obtain the equation

$$\begin{aligned}
&\xi^{-2}\nabla_y \cdot (a(\mathbf{y})\nabla_y u_0(\mathbf{x}, \mathbf{y})) + \\
&+\xi^{-1}\big(\nabla_y \cdot (a(\mathbf{y})\nabla_y u_1(\mathbf{x}, \mathbf{y})) + \nabla_y \cdot (a(\mathbf{y})\nabla_x u_0(\mathbf{x}, \mathbf{y})) + \\
&\quad a(\mathbf{y})\nabla_x \cdot \nabla_y u_0(\mathbf{x}, \mathbf{y})\big) + \\
&+\xi^0\big(\nabla_y \cdot (a(\mathbf{y})\nabla_y u_2(\mathbf{x}, \mathbf{y}) + a(\mathbf{y})\nabla_x u_1(\mathbf{x}, \mathbf{y})) + \\
&\quad a(\mathbf{y})\nabla_x \cdot \nabla_y u_1(\mathbf{x}, \mathbf{y}) + a(\mathbf{y})\nabla_x \cdot \nabla_x u_0(\mathbf{x}, \mathbf{y})\big) + \\
&+\xi^1(\dots) + \cdots + f(\mathbf{x}) = 0
\end{aligned} \tag{2.47}$$

Now, we have to consider that different scales of ξ (if ξ is very small) correspond to different scales of the problem, and thus Eq. (2.47) becomes an infinite system of equations, obtained equating the power-like terms of ξ. The first equation, in the term of ξ^{-2}, is:

$$\nabla_y \cdot (a(\mathbf{y}))\nabla_y u_0(\mathbf{x}, \mathbf{y}) = 0 \quad \text{for } y \ \epsilon \ Y \tag{2.48}$$

from which, given the Y-periodicity of $u_0(\mathbf{x}, \mathbf{y})$, this latter can be expressed as a function of $\mathbf{x}$ alone $u_0(\mathbf{x}, \mathbf{y}) = u_0(\mathbf{x})$, independent of $\mathbf{y}$. This is an important and general result which will be used in the next section in the homogenization of Stokes' law and will also come up again in Chapter 6 in the homogenization of the advection-diffusion equation with particle deposition. Using this result in the following step of the hierarchy of problems

(the one with the term ξ^{-1}), results in

$$\nabla_y \cdot (a(\mathbf{y})\nabla_y u_1(\mathbf{x}, \mathbf{y})) = -\nabla_y \cdot (a(y)\nabla_x u_0(\mathbf{x}, \mathbf{y})) \quad \text{for } y \in Y \tag{2.49}$$

The next step is to express the function $u_1(\mathbf{x}, \mathbf{y})$ only in terms of the function $u_0(\mathbf{x})$. Expanding the derivative in its N dimensions we write the identity

$$\nabla_x u_0(\mathbf{x}, \mathbf{y}) = \sum_{j=1}^{N} \mathbf{e}_j \partial_{x_j} u_0(\mathbf{x}) \tag{2.50}$$

where ∂_{x_j} indicates the differential operator $\frac{\partial}{\partial x_j}$: this notation will henceforward be used, for clarity, throughout the rest of this chapter. Consequently, using this identity in Eq. (2.49),

$$\nabla_y(a(\mathbf{y})\nabla_y u_1(\mathbf{x}, \mathbf{y})) = -\sum_{j=1}^{N} \partial_{y_j} a(\mathbf{y})\partial_{x_j} u_0(\mathbf{x}) \quad \text{for } y \in Y \tag{2.51}$$

At this point in the procedure it is possible to construct the **cell problem**, from which the effective coefficients of the upscaled equation will be calculated. The cell problem is a purely microscale form of the problem under investigation, which means that only those coefficient which are function of only the fast variable $\mathbf{y} = \dfrac{\mathbf{x}}{\xi}$ may appear, and not those with a dependency on the slow variable $\mathbf{x}$.

We then look for a solution to the problem at the scale of ξ^{-1} in the form of

$$u_1(\mathbf{x}, \mathbf{y}) = \sum_{j=1}^{N} w_j(\mathbf{y})\partial_{x_j} u_0(\mathbf{x}) + u_1(\mathbf{x}) \tag{2.52}$$

where $u_1(\mathbf{x})$ is independent of $\mathbf{y}$ and w_j is the Y-periodic solution of the cell problem arising when coupling Eq. (2.52) with Eq. (2.49), which reads as:

$$\nabla_y \cdot (a(\mathbf{y})\nabla_y w_j(\mathbf{y})) = -\nabla_y \cdot (a(\mathbf{y})\mathbf{e}_j) \quad \text{for } y \, \epsilon \, Y, \tag{2.53}$$

since it can be shown that Eq. (2.49) should be satisfied whatever the $\nabla_x u_0(\mathbf{x})$ (more details on this can be found in Hornung (1997) and Auriault and Adler (1995)). Then, proceeding to the terms in ξ^0 in Eq. (2.47) and remembering that the Y-periodic cell is of unitary volume, the following

equation is obtained:

$$\nabla_y \cdot \big(a(\mathbf{y})\nabla_y u_2(\mathbf{x},\mathbf{y}) + a(\mathbf{y})\nabla_x u_1(\mathbf{x},\mathbf{y})\big)+$$
$$a(\mathbf{y})\nabla_x \cdot \nabla_y u_1(\mathbf{x},\mathbf{y}) + a(\mathbf{y})\nabla_x \cdot \nabla_x u_0(\mathbf{x}) + f(x) = 0 \quad \text{for } y \in Y.$$
$$(2.54)$$

Integrating this equation over the volume of Y results in:

$$\int_Y \nabla_y \cdot \big(a(\mathbf{y})\nabla_y u_2(\mathbf{x},\mathbf{y}) + a(\mathbf{y})\nabla_x u_1(\mathbf{x},\mathbf{y})\big)\mathrm{d}y+$$
$$+ \int_Y a(\mathbf{y})\nabla_x \cdot \nabla_y u_1(\mathbf{x},\mathbf{y})\mathrm{d}y+$$
$$+ \int_Y a(\mathbf{y})\mathrm{d}y \Delta_x u_0(\mathbf{x}) + f(x) = 0 \ . \tag{2.55}$$

Using Stokes' theorem (or more precisely the divergence theorem) on the first term of Eq. (2.55), we obtain

$$\int_Y \nabla_y \cdot \big(a(\mathbf{y})\nabla_y u_2(\mathbf{x},\mathbf{y}) + a(\mathbf{y})\nabla_x u_1(\mathbf{x},\mathbf{y})\big)\mathrm{d}y =$$
$$= \int_{\partial Y} \mathbf{n} \cdot \big(a(\mathbf{y})\nabla_y u_2(\mathbf{x},\mathbf{y}) + a(\mathbf{y})\nabla_x u_1(\mathbf{x},\mathbf{y})\big)\mathrm{d}\Gamma(\mathbf{y}), \tag{2.56}$$

where $\mathbf{n}$ is the unit vector normal to ∂Y (which represents the boundary of the volume of the cell Y).

Due to the assumed Y-periodicity of the coefficient functions $u_1(\mathbf{x},\mathbf{y})$ and $u_2(\mathbf{x},\mathbf{y})$, this integral is equal to zero. Then, using a differentiated form of (2.52), namely:

$$\nabla_y u_1(\mathbf{x},\mathbf{y}) = \sum_{j=1}^N \nabla_y w_j(\mathbf{y})\partial_{x_j} u_0(\mathbf{x}) \tag{2.57}$$

in the second term of equation Eq. (2.55), we get:

$$\nabla_x \cdot \nabla_y u_1(\mathbf{x},\mathbf{y}) = \sum_{i,j=1}^N \partial_{y_i} w_j(\mathbf{y})\partial_{x_i x_j} u_0(\mathbf{x}) \ . \tag{2.58}$$

Then finally, rewriting Eq. (2.55),

$$\sum_{i,j=1}^N \int_Y a(\mathbf{y})\partial_{y_i} w_j(\mathbf{y})\partial_{x_i x_j} u_0(\mathbf{x}) + \int_Y a(\mathbf{y})\mathrm{d}y \Delta_x u_0(\mathbf{x}) + f(x) = 0 \ .$$
$$(2.59)$$

For clarity, we can express this in a more compact form using the abbreviation

$$a_{ij} = \int_Y a(\mathbf{y})(\delta_{ij} + \partial_{y_i} w_j(\mathbf{y}))\mathrm{d}y \tag{2.60}$$

thus obtaining the final result:

$$\sum_{i,j=1}^{N} a_{ij}\partial_{x_i x_j} u_0(\mathbf{x}) + f(\mathbf{x}) = 0 \tag{2.61}$$

This equation is the **homogenized** limit of the equation in problem (2.41). For a clearer comparison, we state that the homogenized form of the problem (2.41) is:

$$\begin{cases} \nabla \cdot (A\nabla u(\mathbf{x})) + f(\mathbf{x}) = 0, & x \in \Omega \\ u(\mathbf{x}) = u_{\mathrm{D}}(\mathbf{x}) & x \in \Omega \end{cases} \tag{2.62}$$

or equivalently, that the differential operator $\nabla \cdot (A\nabla u(\mathbf{x}))$ is the homogenization of the operator family $\nabla \cdot (a^\xi(\mathbf{x})\nabla u^\xi(\mathbf{x}))$. The most important step in the passage from the original problem (2.41) to its homogenized form (2.62) is the explicit construction of A, which is obtained, as shown, through the solution of the cell problem (2.53).

Following the procedure which has been just described, a wide range of problems can be tackled. In order to better explain the process, and demonstrate its usefulness with the application to a real case, in the next section a classic result of homogenization will be presented, which is the formal derivation of Darcy's law starting from the microscale Stokes' equation.

2.3.2 From Stokes to Darcy

Media with Obstacles

Before giving the statement of the problem and beginning the homogenization procedure, an important remark has to be done. In the previous section we analysed a very general problem (identified by the family of operators $\mathcal{A}_\xi$) in a medium which was just specified as being periodic, with unit cell Y, but nothing else was assumed about the structure of Y. When one identifies a periodic repeating cell in a porous domain, its most important feature will be its inhomogeneity: even ignoring the particulars of the pore structure, at the very least there will be two phases, a solid and a fluid one. The simplest way (and the one we'll use) to describe this domain is to consider

it an arrangement of periodically spaced obstacles (representing the solid grains). Then, in the single unit cell Y, we'll find a solid grain $\mathcal{G} \subset\subset Y$ with a piecewise smooth boundary Γ. The fluid zone is the remainder of the volume $\mathcal{B} = Y \setminus \mathcal{G}$. This unit cell, as earlier, is repeating periodically on all the domain Ω, and we refer to the whole structure (at the scale of Ω) as, again, being divided in the fluid part

$$\mathcal{B}^{\xi} = \Omega \cap (\xi\mathcal{B}) \,, \tag{2.63}$$

and the solid part

$$\Gamma^{\xi} = \Omega \cap (\xi\Gamma) \,. \tag{2.64}$$

Lastly, in order to have a simpler problem to treat, we'll consider that everywhere in the domain Ω the solid zone has no intersection with the unit cell's Y boundary Γ, or more properly:

$$\partial\Omega \cap \Gamma^{\xi} = \varnothing \tag{2.65}$$

This is an important assumption that will be useful in the following calculations. This geometric description can also be visually found, for clarity, in Figg. 2.2 and 2.3.
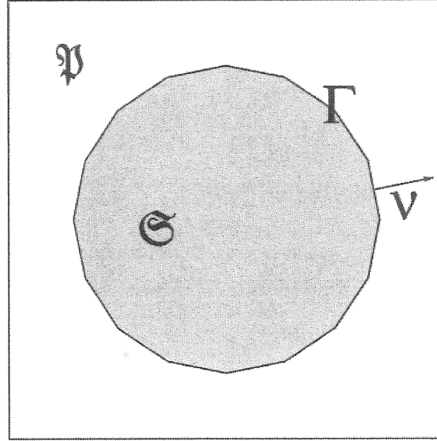
Figure 2.2: Microscopic periodic unit cell, with fluid domain $\mathcal{B}$, solid domain $\mathcal{G}$ and grain surface Γ in evidence. Image from Hornung (1997).

Having modified the structure of the domain, the problem to be solved also changes. For example, the corresponding problem to (2.41) in this
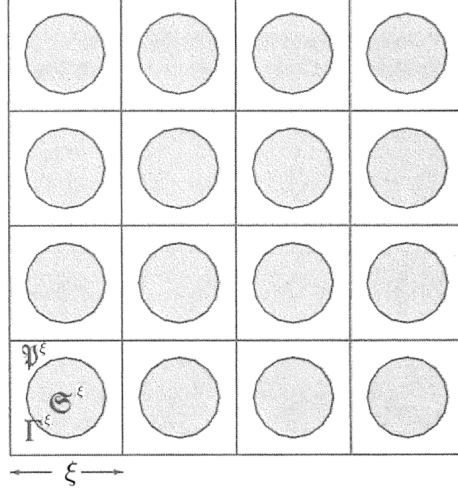
Figure 2.3: Structure of the macroscale domain, constituted by an arrangement of periodically repeating unit cells, each with dimension $l = \xi L$. Image from Hornung (1997).

domain is the following.

$$\begin{cases} -\nabla \cdot (a^\xi(\mathbf{x})\nabla u^\xi(\mathbf{x})) = f(\mathbf{x}) & x \in \mathcal{B}^\xi \\ \mathbf{n} \cdot a^\xi(\mathbf{x})\nabla u^\xi(\mathbf{x}) = 0 & x \in \Gamma^\xi \\ u(\mathbf{x}) = u_{\mathrm{D}}(\mathbf{x}) & x \in \partial\Omega \end{cases} \tag{2.66}$$

where now the domain of a^ξ is just the fluid zone $\mathcal{B}$. The steps towards the homogenization of this problem are similar to the ones performed in the previous section, and can be found in full in Hornung (1997) and Zhikov et al. (1994).

Homogenization of Stokes equation

We start from Stokes' flow and continuity equations in a periodic porous medium (refer to Figg. 2.2 and 2.3) with a no-slip (Dirichlet) condition on the boundary of solid pores:

$$\begin{cases} \xi^2 \mu \nabla^2 \mathbf{v}_\xi(\mathbf{x}) - \nabla p_\xi(\mathbf{x}) = 0 & x \in \mathcal{B}^\xi \\ \nabla \cdot \mathbf{v}_\xi(\mathbf{x}) = 0 & x \in \mathcal{B}^\xi \\ \mathbf{v}_\xi(\mathbf{x}) = 0 & x \in \Gamma^\xi \end{cases} \tag{2.67}$$

This differs from the usual statement of Stokes equation, having scaled the viscosity μ by a factor of ξ^2. This is done in order to ensure that the velocity $\mathbf{v}_\xi$ has a nontrivial limit as the scale factor ξ goes to zero. The linearity of the equations allow this scaling as it is always possible to replace $\mathbf{v}_\xi$ with $\xi^2\mathbf{v}_\xi$. Phisically speaking, the now very small viscosity $\xi^2\mathbf{v}_\xi$ balances exactly the friction on the walls of the solid grains due to the no-slip boundary condition. More details on this can be found in Hornung (1997) and Allaire (1989).

Then, both velocity $\mathbf{v}_\xi$ and pressure p_ξ are expanded asymptotically, as per Eq. (2.43), resulting, respectively, in:

$$\mathbf{v}_\xi(\mathbf{x}) = \mathbf{v}_0(\mathbf{x}, \mathbf{y}) + \xi\mathbf{v}_1(\mathbf{x}, \mathbf{y}) + \xi^2\mathbf{v}_2(\mathbf{x}, \mathbf{y}) + \ldots \,, \tag{2.68}$$

and

$$p_\xi(\mathbf{x}) = p_0(\mathbf{x}, \mathbf{y}) + \xi p_1(\mathbf{x}, \mathbf{y}) + \xi^2 p_2(\mathbf{x}, \mathbf{y}) + \ldots \,. \tag{2.69}$$

where the coefficient functions are periodic with period Y. Using the differentiation rules of Eq. (2.46), we have the system

$$\begin{cases} \xi^0\mu\nabla_y^2\mathbf{v}_0(\mathbf{x}, \mathbf{y}) + \xi^1(\ldots) + \cdots = \\ \quad = \xi^{-1}\nabla_y p_0(\mathbf{x}, \mathbf{y}) + \xi^0 \left(\nabla_y p_1(\mathbf{x}, \mathbf{y}) + \nabla_x p_0(\mathbf{x}, \mathbf{y})\right) & y \in \mathcal{B} \\ \xi^{-1}\nabla_y \cdot \mathbf{v}_0(\mathbf{x}, \mathbf{y}) + \xi^0 \left(\nabla_y \cdot \mathbf{v}_1(\mathbf{x}, \mathbf{y}) + \nabla_x \cdot \mathbf{v}_0(\mathbf{x}, \mathbf{y})\right) + \\ \quad + \xi^1(\ldots)\cdots = 0 & y \in \mathcal{B} \\ \xi^0\mathbf{v}_0(\mathbf{x}, \mathbf{y}) + \xi^1\mathbf{v}_1(\mathbf{x}, \mathbf{y}) + \cdots = 0 & y \in \Gamma \end{cases} \tag{2.70}$$

Then, new expressions equating the power-like terms of ξ are written, starting from the lowest order. The ξ^{-1} term of the expanded Stokes' equation reads

$$\nabla_y p_0(\mathbf{x}, \mathbf{y}) = 0 \qquad\qquad y \in \mathcal{B} \,, \tag{2.71}$$

from which it follows that $p_0(\mathbf{x}, \mathbf{y})$ is independent of y, $p_0 = p_0(\mathbf{x})$. This results is coherent with the actual physical case, where pressure can be considered as a superposition of slow large scale variations, and fast microscale oscillations: this is the sense of the expansion Eq. (2.69). The next term, in ξ^0, reads

$$\mu\nabla_y^2\mathbf{v}_0(\mathbf{x}, \mathbf{y}) = \nabla_y p_1(\mathbf{x}, \mathbf{y}) + \nabla_x p_0(\mathbf{x}, \mathbf{y}) \qquad y \in \mathcal{B} \,, \tag{2.72}$$

while the $\xi^{-}1$ term in the expanded continuity equation is

$$\nabla_y \cdot \mathbf{v}_0(\mathbf{x}, \mathbf{y}) = 0 \qquad\qquad y \in \mathcal{B}\,. \qquad\qquad (2.73)$$

Then, similarly to Eq. (2.50),

$$\nabla_x p_0(\mathbf{x}) = \sum_j \mathbf{e}_j \partial_j p_0(\mathbf{x}) \qquad\qquad (2.74)$$

At this point it is possible to construct the following family of cell problems,

$$\begin{cases} \nabla_y^2 \mathbf{w}_j(\mathbf{y}) = \nabla_y \pi_j(\mathbf{y}) - \mathbf{e}_j & y \in \mathcal{B} \\ \nabla \cdot \mathbf{w}_j = 0 & y \in \mathcal{B} \\ \mathbf{w}_j(\mathbf{y}) = 0 & y \in \Gamma \end{cases} \qquad (2.75)$$

having as solutions the Y-periodic vector fields $\mathbf{w}_j(\mathbf{y})$, and where $\pi_j(\mathbf{y})$ are the corresponding pressure fields. Solving these cell problems, the following result is obtained:

$$\mathbf{v}_0(\mathbf{x}, \mathbf{y}) = -\frac{1}{\mu} \sum_j \mathbf{w}_j(\mathbf{y}) \partial_j p_o(\mathbf{x}). \qquad\qquad (2.76)$$

Then, we can define the average of this vector field as

$$\bar{\mathbf{u}}(\mathbf{x}) = \int_{\mathcal{B}} \mathbf{v}_0(\mathbf{x}, \mathbf{y}) \mathrm{d}y \,, \qquad\qquad (2.77)$$

whose i-th component is

$$\bar{\mathbf{u}}_i(\mathbf{x}) = -\frac{1}{\mu} \sum_j k_{ij} \partial_{x_j} p_0(\mathbf{x}) \,, \qquad\qquad (2.78)$$

with

$$k_{ij} = \int_{\mathcal{B}} w_{ji}(\mathbf{y}) \mathrm{d}y. \qquad\qquad (2.79)$$

For compactness, the tensor $K = (k_{ij})_{i,j}$ is introduced, leading to

$$\bar{\mathbf{u}}(\mathbf{x}) = -\frac{1}{\mu} K \nabla p_0(\mathbf{x}) \qquad\qquad (2.80)$$

which is the familiar form of *Darcy's law*. It can also be shown that the vector field $\bar{\mathbf{u}}$ is divergence-free, completing the upscaling. This detail and a more in-depth description of this procedure can be found in Hornung (1997),

Palencia (1980) and Tartar (1980).

Equation (2.80) constitues a very important result, as it gives one of the few mathematically solid justifications for the most widely known empirical law in the field of flow in porous media, and serves to show the method's capabilities in treating the upscaling of transport problems. In Chap. 6 this method will be used to work on the upscaling of the superficial reaction (deposition) problem described earlier in this chapter, central to this thesis.

Chapter 3

Scalar and particle dispersion

In this chapter fluid flow and scalar/ particle transport and dispersion through a three-dimensional model of a porous medium will be described, by means of CFD simulations with finite-volume method discretization (FVM). Moreover, this work has the purpose of developing and validating reliable computational tools for the efficient pore-scale simulation in complex geometries, accompanied by the choice of adequate numerical methods and grid convergence tests, as currently done in computational fluid dynamics analysis. There are a number of novel points in this work, with respect to other works recently appeared in the literature. In this work the full Navier-Stokes equation is solved, instead of solving the simpler Stokes equation (often adopted in this context). Secondly, instead of considering a porous structure (obtained "in-silico" with a ballistic physics algorithm) composed of monodisperse spheres, in this work the porous medium has been generated by randomly packing non-spherical highly irregular non-convex polydisperse objects, whose shape and size distribution have a direct link to experimentally characterized sands. Another important novelty of this work is that this operation is conducted here by using for the first time the open-source computer graphics three-dimensional code Blender. This code can easily overcome the limitations of other codes, that are limited to the treatment of spheres and convex objects. In addition to this, particular attention is paid here to the well-known numerical issues related to mesh generation and spatial discretization encountered when the Navier-Stokes and the advection-diffusion equation are solved with the finite-volume method, which play an important role in determining the final accuracy of the finite-volume scheme and are often overlooked. This is done here by using the open-source CFD


The content of this chapter, in a modified form, has been published in Icardi et al. (2014)

code `OpenFOAM`. Another point worth of notice, beyond the fully open-source computational tools, is the usage of an "Eulerian" method to analyze solute dispersion at the pore-scale. We will show that this approach, in contrast to the commonly used tracer particle "Lagrangian" approach, has many computational and practical advantages. The manuscript is organized as follows. First the computational tools developed to extract grain information from real images, reconstruct realistic geometries and discretize the pore space are described. Subsequently the numerical details about the pore-scale simulations are reported together with the results. Simulation predictions are eventually processed to extract velocity distributions and dispersion coefficients, as well as to assess the validity of the Fick law to describe dispersion phenomena. Conclusions and possible next steps are discussed in the last section.

3.1   Test cases and operating conditions

In this section the strategy employed to create the three-dimensional porous medium used in this work and the mesh generation procedure for performing the finite-volume discretization are briefly described.
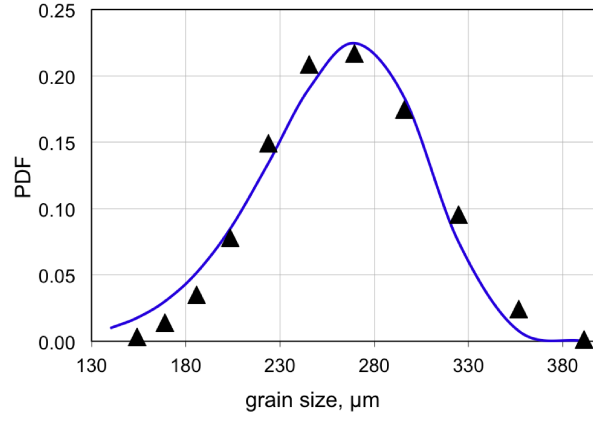
3.1.1   Grain packing generation
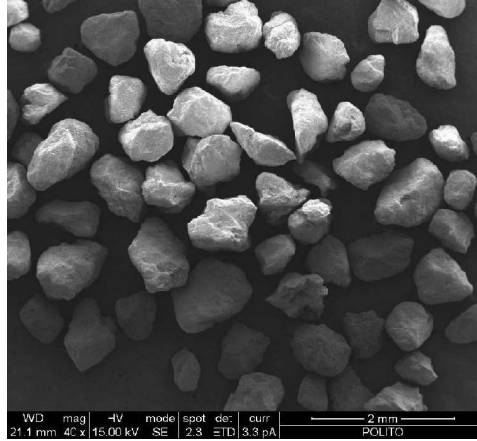
Figure 3.1: SEM image of the real sand sample used to extract grain size distribution and approximate the grain shapes.

The first necessary step requires to build a representative microscopic model of a porous medium sample in order to simulate fluid flow in these

Figure 3.2: Grain size distribution of the sand packing under study (filled triangles) and approximation with Weibull distribution (continuous blue line).
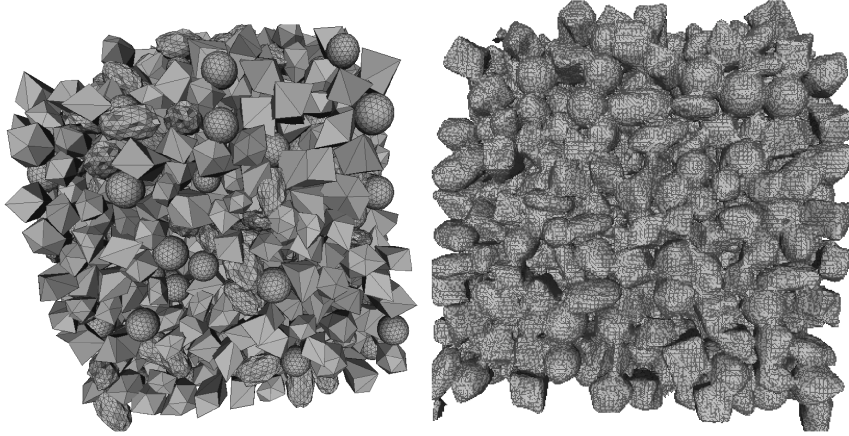
Figure 3.3: Mesh re-sampling, randomization and regularization. Original surface mesh (left) and re-sampled mesh (right).

systems. There are many ways to obtain such a model: the first choice is between real sand sample images, for example experimentally acquired by micro-computer tomography techniques, and realistic reconstructions by means of suitable algorithms (Blunt et al., 2013). Although the former provides representations of the pore microstructure which are real, the extraction procedures (segmentation, surface reconstruction, etc.) are usually quite complicated, expensive and with a high degree of arbitrariness. Therefore, it was chosen to reconstruct a realistic porous medium with ad-hoc algorithms. It has to be noted that when following this approach one has to make sure that the characteristics and features of the generated porous medium (e.g. porosity, grain size distribution and pore-throat structure) are representative of a real system. Notwithstanding these difficulties, there are several advantages with this approach; it is possible, for example, to test simple geometries (where real grains are modeled as spheres) that make it easier to study multiple test cases (e.g. models with different grain diameter or porosity) in a semi-automatic fashion (Boccardo et al., 2014b), as it will be shown in Chapter 5 of this thesis.

A number of methods have been proposed to synthetically generate realistic packed geometries. Some of them are based on the idea of representing the medium with a pore-network model, whereas some others "reconstruct" the entire structure of the porous medium, down to the single grains, using different algorithms (i.e. random sequential adsorption, gravitational deposition, collective arrangement, binary random fields) (Feder, 1980; Pilotti, 1998; Yeong and Torquato, 1998; Øren and Bakke, 2002; Koutsourelakis and Deodatis, 2005; Adler and Taylor, 2007). In this work, two different methods of packing generation, both based on the open-source library Bullet Physics (Coumans, 2006), were tested: SettleDyn (Blöcher and Zimmermann, 2008) and Blender (Van Gumster, 2009). The tested methods simulate the sedimentation of real three-dimensional grains, represented by convex polygonal surface meshes, generating loose sand-like structures from given particle forms and grain size distributions.

The first step is the definition of grain shape and grain size distribution, that in this work were obtained respectively by two-dimensional scanning electron microscopy (SEM) scans (see for example Fig. 3.1) and static-light scattering measurements carried out on standard sand samples. For the case investigated in this work the final mean grain size d_{50} was equal to 0.277 mm. The grain size distribution was then fitted with a Weibull distribution (Boccardo et al., 2014b; Tosco et al., 2013) and was then randomly sampled when creating the packing. Figure 3.2 compares the experimentally measured grain size distribution of the sample with the reconstructed Weibull

distribution.

Different confined packings of thousands of grains were then generated, by randomly sampling the Weibull distribution, on a single core machine, with large quantity of memory in a few hours. These tests highlighted, for the operating conditions investigated in this work, a higher flexibility when using Blender, especially in terms of robustness and convergence. One of these packings (created with Blender) with more than 3000 grains, was extensively used in this work for most of the pore-scale simulations. The final optimized porous medium is a cube domain of 2.1 mm length and is characterized by an average porosity of 0.35. By splitting the geometry in ten sub-volumes along the x-axis, it was noted that the porosity (in these sub-volumes) fluctuates around this value by approximately 1%, while the porosity calculated on the surfaces (between each subsequent sub-volume) varies between 0.31 and 0.39.

3.1.2 Mesh generation

After the generation of the grain packing, the geometric representation (made of polygonal surface mesh) of the resulting grain packings was cleaned through mesh re-sampling, in order to remove intersections and artifacts. This was done with the marching cubes algorithm (Lorensen and Cline, 1987; Cignoni et al., 2008). An example is reported in Fig. 3.3, that shows a surface mesh, obtained with the algorithms previously described and grains characterized by very sharp edges, and the final re-sampled mesh. After re-sampling the pore domain is ready to be discretized through body-fitted meshes, as commonly done when the FVM is used.

As mentioned before, great care was put forward during the pre-processing phase of this work in order to ensure the highest possible accuracy with respect to numerical and computational issues. A careful analysis of the mesh generation process now follows, along with the description of the steps taken to ascertain the validity of the final mesh thus obtained.

The mesh utility `snappyHexMesh`, native to the open-source package `OpenFOAM` (OpenCFD, 2013), was used. Grid building was performed in two steps. First, a structured, cartesian mesh was created in the fluid portion of the domain, in order to minimize average non-orthogonality and skewness in the final mesh. The handling of the actual surface of the solid part in this initial step is done in a way similar to how immersed boundary meshes are constructed, resulting in a step-wise approximation of the grains. However, a precise reconstruction of the actual grain geometry was deemed essential in this work, thus requiring a second step in which the mesh was modified

by means of relocating boundary vertices, resulting in a body-fitted mesh. A visual aid for the description of this process is found in Fig. 3.4.
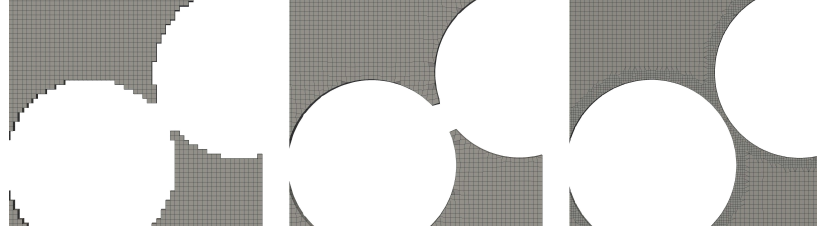

Figure 3.4: Details of the mesh refinement process. Step-wise castellation (left), body-fitting via vertices moving (center) and precise geometry reconstruction with subsequent mesh refinements (right).

In addition to these two steps, one of the subsequent grid refinement steps is also visualized. In fact, the most critical operation was the construction of a mesh of high quality to ensure grid-independent results. To this end, a number of refinements were performed, and two parameters monitored throughout in order to quantitatively assess the resulting mesh suitability for use with the CFD code. Given the heavy computational resources required for the CFD calculations (as described in the following sections), these tests were not performed on the full domain used for the production runs, but rather on two smaller sub-volumes. The linear dimensions of each of these volumes are smaller by a factor of four with respect to the complete geometry, resulting in 500 μm $\times$ 500 μm $\times$ 500 μm cubes. This is shown in Fig. 3.5.

Case	Mesh cells (thousands)	ϵ (-)	D_g^* (μm)
coarse grid	37	0.3025	203.0
unif. ref.	308	0.3088	207.8
near-grain ref. 1	1 218	0.3102	217.4
near-grain ref. 2	2 284	0.3104	214.9
near-grain ref. 3	3 539	0.3105	216.1
near-grain ref. 4	5 053	0.3105	215.6

Table 3.1: Number of mesh cells, porosity and effective grain diameter (μm) for each of the grid refinement steps.

An outline of all the mesh modification steps, along with the calculated relevant parameters associated with each test (for one of the two sub-volums), is reported in Tab. 3.1. As a qualitative description of these cases, the first represents a coarse grid, whereas the second is obtained after a
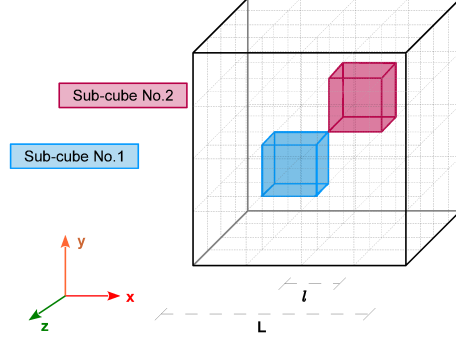
Figure 3.5: Complete geometry bounding box and location of the two sub-volumes chosen for the grid independence analysis.

uniform refinement across the computational domain. The following cases (near-grain ref. 1, 2, 3 and 4) differ by representing progressive refinements of mesh cells size near the border of the grains, with this region being chosen in order to increase the precision in the description of the momentum and particle concentration boundary layers, where the gradients of these properties will be stronger. The first of the two properties of interest being monitored at this stage is the porosity: as it can be seen from Tab. 3.1 its value changes (increasing slightly) with the increase in the number of cells. This is due to the addition of more cells near the surface of the grains allowing not only for a better numerical solution, but also for a more precise reconstruction of the actual porous medium geometry. Again, Fig. 3.4 exemplifies this process. The fourth case (near-grain ref. 2) reaches a satisfactory description in such respect. The other parameter needed to assess the grid independence of the results for the flow field is the equivalent diameter D_g^*. Following the same methodology applied in a previous work (and described in details therein (Boccardo et al., 2014b)), for each level of grid refinement steady-state flow field simulations at different superficial velocities were run, and the pressure drop results compared with the predictions of the Ergun law for that system (see Eq. (2.12)). Treating the grain diameter as a fitting parameter, the effective diameter D_g^* reported in Tab. 3.1 results from the closest fitting of the obtained CFD results with the theoretical predictions. Considering the variation of D_g^* with increasing mesh cells number, again the fourth case provides a good resolution of the momentum boundary layer, as

the heavy mesh refinements performed in the subsequent cases correspond to negligible changes in effective grain diameter. Thus, the mesh for the complete geometry used in the final runs, from which all the results presented in this work were obtained, was built in such a way to result in the same features as those identified in the case (near-grain ref. 2) of Tab. 3.1.

3.1.3   Numerical details of the CFD simulations

The flow field in the reconstructed geometry was simulated with the open-source code `OpenFOAM`. The three-dimensional incompressible steady Navier-Stokes equations were solved with the `simpleFoam` solver. As mentioned the equations were discretized with the FVM. The numerical schemes used were chosen in order to minimize the numerical errors for the different test cases characterized by a wide range of Reynolds numbers (see Table 3.2). A second-order central scheme with limiters to avoid oscillations was used for spatial discretization and the SIMPLEC scheme was used to overcome the pressure-velocity coupling problem.

The whole cubic domain, extracted by the packing and reported in Figs. 3.3 and 3.5, was studied with a fixed hydraulic head drop between inlet and outlet and with symmetric conditions on the lateral boundaries. On these boundaries it is imposed that the derivatives of the velocity components along the orthogonal direction are null and that the orthogonal velocity component is also null. For example, for the two boundaries orthogonal to the y-axis: $V_y = 0$, whereas V_x and V_z are kept free; the same conditions hold also for the boundaries orthogonal to the z-axis. This means that the resulting main flow is directed along the x-axis and there is no flow escaping from lateral boundaries (in the y and z directions). The problem of the best boundary conditions was also investigated in previous works from the author and co-workers (as explained more in detail in Chap. 5), where it was shown that this set of conditions resulted in the least invasive approach, that could avoid the use of pre- and post-mixing conditions, as well as the exclusion of the external part of the flow from the statistical analysis (Tosco et al., 2013; Boccardo et al., 2014b). The simulated domain length was $\mathcal{L}_x = \mathcal{L}_y = \mathcal{L}_z = 2$ mm and it contained about three thousands sand grains. For each value of hydraulic head drop, the mean flow rate and Darcy fluxes U_x were calculated in sections of the porous medium orthogonal to the mean flow field. A summary of the resulting Reynolds, $\mathrm{Re} = D_g^* q / \varepsilon \nu$, and Péclet numbers, $\mathrm{Pe} = D_g^* q / \varepsilon \mathcal{D}$, is reported in Table 3.2; both dimensionless numbers are evaluated by using $D_g^* = 0.270$ mm as en estimation of the grain size D_g. As it is seen, the flow fields obtained at different Reynolds

numbers were used to transport an Eulerian scalar/particle concentration field with different diffusion coefficients resulting in Péclet numbers ranging from 10^{-2} up to 10^6. As already mentioned this coefficient corresponds to molecular diffusion for scalars and to the Brownian diffusion coefficient for particles.

The simulations of the flow field were carried out in parallel on a Linux workstation with 12 Intel Xeon X6960 cores. The computational bottle-neck for these simulations turned out to be the huge memory usage (100GB), rather than the convergence iterations (usually less than 100). In our configuration this resulted in 12 hours of total CPU time for each flow field computation.

The simulations of solute transport were carried out in `OpenFOAM` but with a unsteady solver, up to the full saturation of the medium. A constant concentration (constant Dirichlet boundary conditions with a fixed concentration equal to unity) was employed as boundary condition at the inlet. A null concentration gradient was instead used as boundary condition on the grain surfaces (neglecting therefore particle deposition) and on the lateral and outlet boundaries (approximating an infinite medium).

It is worth mentioning here that the grid independence study conducted in the previous section, should be repeated also for the solute dispersion simulations, in order to ensure that not only the predicted flow field is grid-independent, but also that grid independence holds for the solute concentration field. A computational grid resulting in a grid-independent flow field, may not result in a grid-independent solute concentration field, because the solute concentration gradients occur on length-scales smaller than the those of momentum, when the Schmidt number, Sc, is greater than one. Although the computational grids should be refined accordingly, the grid used to obtain a grid-independent flow field oftentimes results in a grid-independent solute concentration field. This condition will certainly hold here, where there is not a solute concentration boundary layer to resolve, as the solute is not reacting on the grain surface, but is simply advected and diffused and therefore gradients at the pore-scale are not very large.

These more computationally demanding simulations were carried out in parallel on the Curie supercomputer, owned by GENCI and operated by CEA, using 48 Intel Nehalem-EX X7560 cores. In our configuration this resulted in 240 hours of total CPU time for each scalar transport computation. The domain was decomposed by simply splitting the domain in each direction by powers of two. Scalability tests were performed for the flow solver and for the scalar transport, showing that, even if the three-dimensional mesh is highly irregular and unstructured, it is possible to reach an almost

linear speed-up up to 512 cores, excluding the I/O operations. Due to the high Péclet number flows a second-order limited upwind space discretization with second-order Crank-Nicholson time stepping was used to solve the solute concentration transport equation (i.e. Eq. (2.14)).

q (m s^{-1})	Re	Pe		
		$\mathcal{D} = 5 \times 10^{-9}$ (m^2 s^{-1})	$\mathcal{D} = 5 \times 10^{-10}$ (m^2 s^{-1})	$\mathcal{D} = 5 \times 10^{-11}$ (m^2 s^{-1})
1.2×10^{-7}	9.6×10^{-5}	1.9×10^{-2}	1.9×10^{-1}	1.9×10^{0}
1.2×10^{-6}	9.6×10^{-4}	1.9×10^{-1}	1.9×10^{0}	1.9×10^{1}
1.2×10^{-5}	9.6×10^{-3}	1.9×10^{0}	1.9×10^{1}	1.9×10^{2}
1.2×10^{-4}	9.6×10^{-2}	1.9×10^{1}	1.9×10^{2}	1.9×10^{3}
1.2×10^{-3}	9.6×10^{-1}	1.9×10^{2}	1.9×10^{3}	1.9×10^{4}
1.2×10^{-2}	9.2	1.8×10^{3}	1.8×10^{4}	1.8×10^{5}
8.3×10^{-2}	66	1.3×10^{4}	1.3×10^{5}	1.3×10^{6}
3.9×10^{-1}	314	6.1×10^{4}	6.1×10^{5}	6.1×10^{6}

Table 3.2: Superficial flow velocities, q, Reynolds numbers, Re, molecular diffusion coefficients, $\mathcal{D}$, and resulting Péclet numbers, Pe.

## 3.2 Results and discussion

In what follows the results of our simulations are presented, focusing first on the flow field predictions, and subsequently on the solute transport predictions.

3.2.1 Fluid flow

Figure 3.6 reports a typical example of the flow field inside the porous medium for a Reynolds number of 9.6×10^{-3}. We begin our analysis by plotting the normalized pressure drops, $\Delta P / \rho q^2 \mathcal{L}_\mathrm{x}$, versus the normalized Darcy velocity, q/ν, resulting in the well known behavior reported in Fig. 3.7. As expected two domains are identified, one at low Darcy flux values corresponding to the region of validity of the Darcy law (and a linear behaviour in this graph), and a second one at higher values of Darcy flux where this law is not valid anymore. From the slope of the curve (in the first linear region) an intrinsic permeability of 4.0×10^{-8} cm^2 can be obtained. By using Eq. (2.22), the tortuosity, τ, was estimated in our case to be equal to 1.2 for low Re. However, for Reynolds numbers greater than ten it increases and reaches the value of 1.7 for Re = 314. This is due to the different

flow conditions in the pore space arising at higher velocities, changing the trajectories of the moving fluid and thus τ.
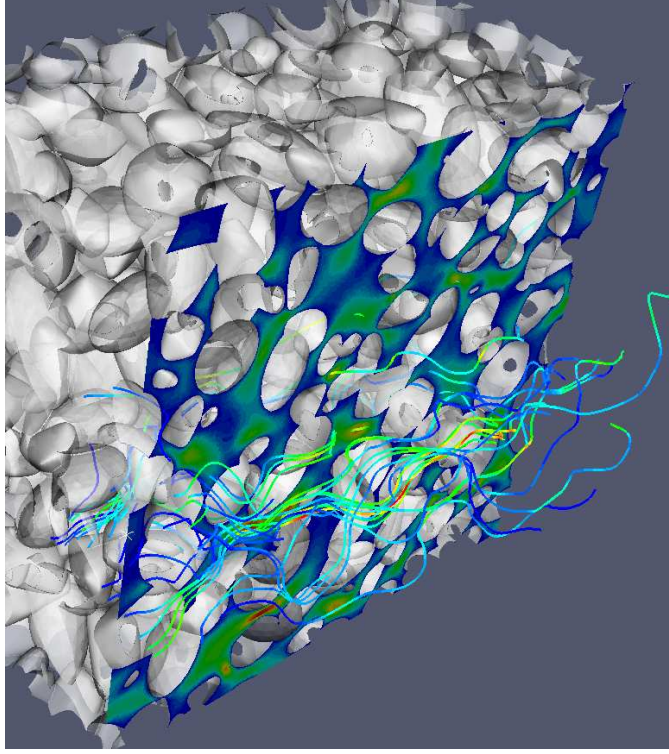
Figure 3.6: Visualization of the flow field in the porous medium for Re $= 9.6 \times 10^{-3}$. Velocity magnitude is computed in a central slice and some flow streamlines are shown. Color coding from blue to red: 0 - 2.5×10^{-6} m s^{-1}.

Further analysis of the simulation data requires some upscaling, for which different methodologies were proposed and we refer to the work of Cushman et al. (2002) for an overview. In the present work simulation results were analyzed by both volume-averaging on the whole three-dimensional domain and by surface-averaging on ten equispaced sections orthogonal to the main flow direction x. In addition to that these ten surfaces were also used to evaluate how relevant properties are spatially distributed.

For example, by analyzing how the fluid velocity differs from point to point on these ten surfaces, the data reported in Fig. 3.8 and Fig. 3.9 were obtained. These figures show the velocity distributions for the x, y and z fluid velocity components, in three of the ten sections investigated, for two superficial velocities, resulting in Reynolds numbers of Re $= 9.6 \times 10^{-3}$ and of Re $= 66$, respectively. The histograms were computed with 1000 samples
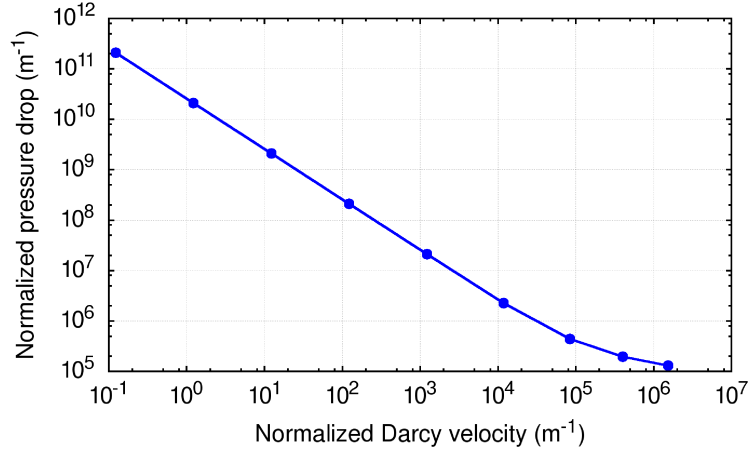
Figure 3.7: Normalized pressure drops, $\Delta P/\rho q^2 \mathcal{L}_{\mathrm{x}}$, versus normalized superficial velocity, q/ν. The slope of the first part of the curve represents the inverse of the permeability of the medium.

on each surface and are reported in logarithmic scale. It is worth mentioning that excluding from the analysis the external portion of the flow (to reduce the possible effects of boundary conditions) does not significantly change the results. As it is possible to see from Fig. 3.8, the velocity distribution for the x component has a maximum corresponding to the superficial velocity, V_x, but highlights in the section regions where the fluid moves with different velocities. Comparison of these distributions with the equivalent Gaussian distributions (that share the same mean and variance) highlights a much higher frequency of velocities close to the mean value and, at the same time, the existence of larger tails of the distributions. Closer observation of the distributions in the y and z directions leads to similar conclusions, with the only difference that now these distributions are centered on zero (as there is no net flux in these directions) and exhibit a certain symmetry and a shape slightly closer to that of a Gaussian distribution. When the superficial velocity is increased the situation observed is very similar (see Fig. 3.9) to the previous one, as in this case the distributions are characterized by larger variances. Comparison of Fig. 3.8 with Fig. 3.9 also highlights that when Re is low, the distributions are very skewed and almost every fluid element in the section moves with $V_x > 0$. However, When Re = 66, noticeable fractions of the section show negative values for V_x; this is an indication of high-Re circulation inside the porous medium, as also indicated by other authors (Hill and Koch, 2002; Hill et al., 2001b,a).
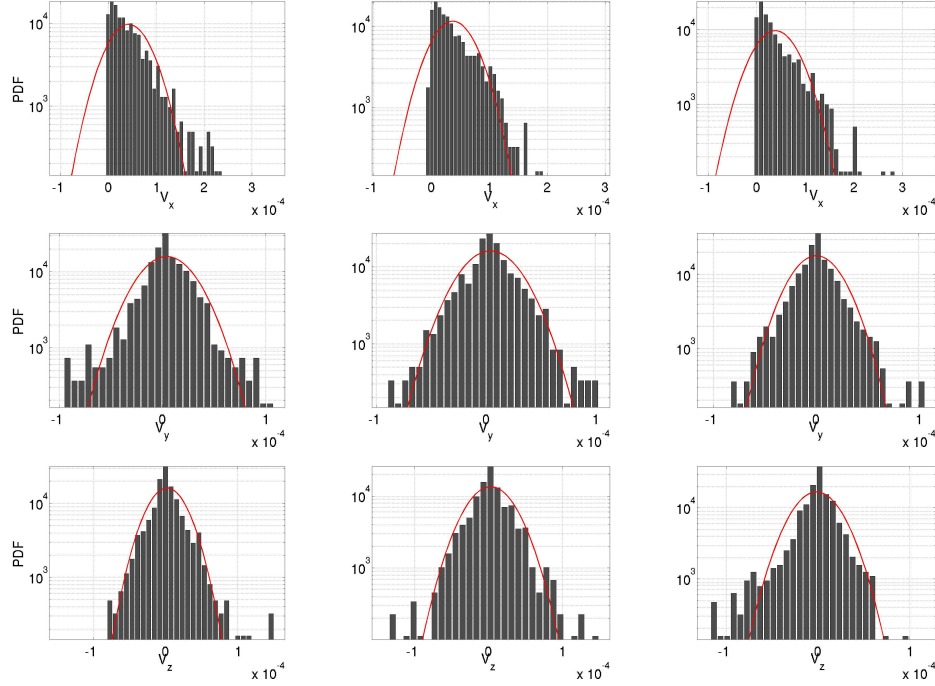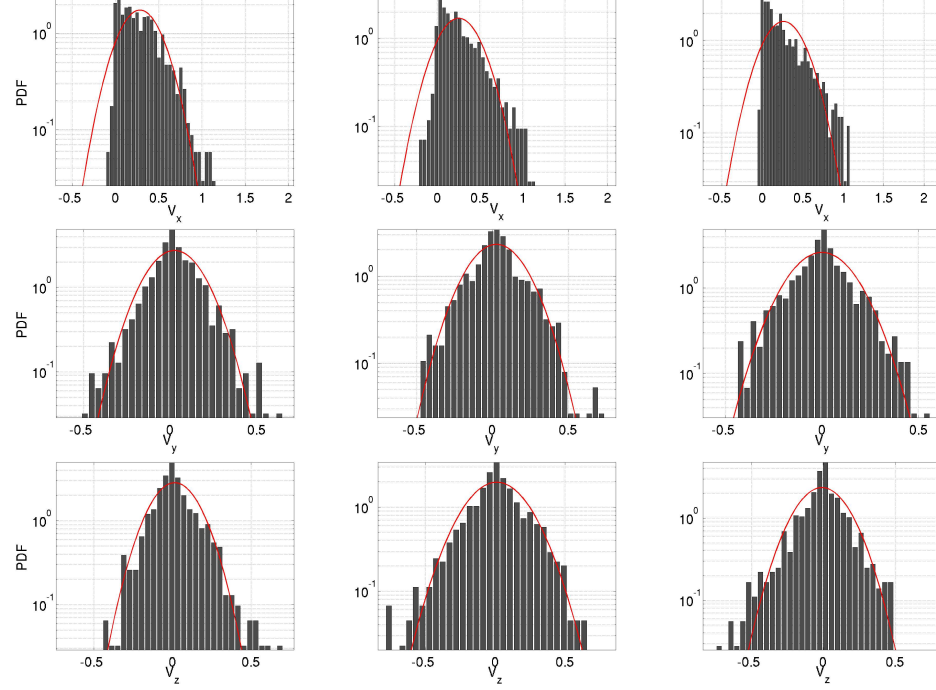
Figure 3.8: Probability density functions $(\mathrm{m^{-1}\,s})$ for $\mathrm{Re} = 9.6 \times 10^{-3}$ and for, from top to bottom, the x-, y-, and z-velocity components $(\mathrm{m\,s^{-1}})$ and for, from left to right, the first, fourth and tenth section. The histogram corresponds to the actual distribution as calculated from the simulations, whereas the red curve is the Gaussian distribution with identical mean and variance.

3.2.2 Hydrodynamic dispersion

To quantify the effect of these distributions in generating dispersion phenomena in the porous medium, let us analyze the results of the solution dispersion simulations. One typical result is reported in Figure 3.10, where the normalized solute concentration at three instants of the simulation is reported. As it is seen, as the solute moves downstream hydraulic dispersion takes place and the concentration front becomes more and more smoothed out.

As already said, the three-dimensional results were surface-averaged on sections perpendicular to the main flow direction, and, among other variables, the average solute concentration in these sections was tracked versus time. The resulting time-evolution curves (known as breakthrough curves) were then used to characterize the dispersion dynamics in the medium. Three typical results for different Re and Pe numbers are reported in Fig. 3.11, for nine equidistant sections, from $x = 0.15\mathcal{L}_{\mathrm{x}}$ to $x = 0.95\mathcal{L}_{\mathrm{x}}$ (to avoid

Figure 3.9: Probability density functions (m^{-1} s) for Re = 66 and for, from top to bottom, the x-, y-, and z-velocity components (m s^{-1}) and for, from left to right, the first, fourth and tenth section. The histogram corresponds to the actual distribution as calculated from the simulations, whereas the red curve is the Gaussian distribution with identical mean and variance.
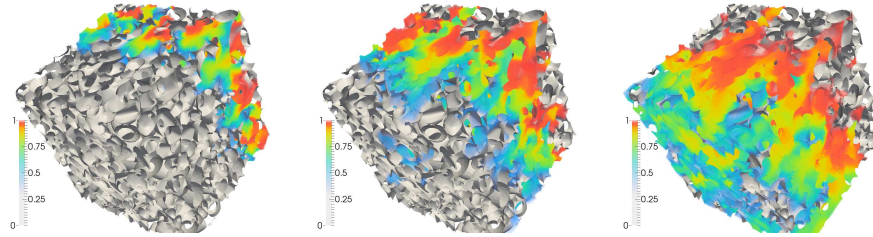
Figure 3.10: Contour plots of the solute dimensionless concentration in the porous medium at three instants of the simulation for Pe = 1.9×10^3.

boundary effects).

The breakthrough curves reported in Fig. 3.11 with continuous lines correspond to three different regimes. In the first one (top) molecular diffusion is prevailing over advective transport, in the second and third ones (middle) the two effects are of the same order of magnitude, while in the fourth one (bottom) molecular diffusion can be neglected with respect to advection. Due to the small changes in porosity of the sections, some of the curves of contiguous sections overlap.

The concentration transport at the macroscale (as sketched in Fig. 3.11) should obey to the macroscopic advection-diffusion equation reported in its general form in (2.16) and for the problem investigated in this work, Eq. (2.16) takes the one-dimensional form reported in Eq. (2.20), whose coefficients are in turn unknown. Neglecting the presence of a possible stagnant phase or a retardation factor, the only actual unknown parameter is the hydrodynamic dispersion. However, also the effective transport velocity (U_{eff}) was included as a unknown parameter, to check the validity of the transport equation. Since we are considering a volume comparable to the representative elementary volume (i.e.: the smallest volume representative of the macroscale characteristics of the porous medium), there are not enough data along the x-direction, but temporal data can be indeed considered (for fixed spatial locations).

The two unknown parameters (i.e. U_{eff} and D) were computed with two methods. The first method is based on the inverse problem formulation. Given the breakthrough curves (concentration over time), the effective parameters are estimated with non-linear least square minimization using standard optimization techniques. The second strategy is instead based on the method of moments (Aris, 1956), where the unknown parameters are calculated from the first three normalized centered temporal moments at the outlet of the computational domain:

$$
\begin{aligned}
M_0 &= \int_0^\infty g(x = \mathcal{L}_{\text{x}}, t) \, \mathrm{d}t; \\
M_1 &= \int_0^\infty \frac{g(x = \mathcal{L}_{\text{x}}, t)t}{M_0} \, \mathrm{d}t; \\
M_2 &= \int_0^\infty \frac{g(x = \mathcal{L}_{\text{x}}, t)t^2 \, \mathrm{d}t}{M_0} - M_1^2,
\end{aligned}
\tag{3.1}
$$

where $g(x, t)$ is the Green function of Eq. (2.16) (i.e. the solution for a Dirac delta boundary condition centered at $x = 0$ and $t = 0$). The effective
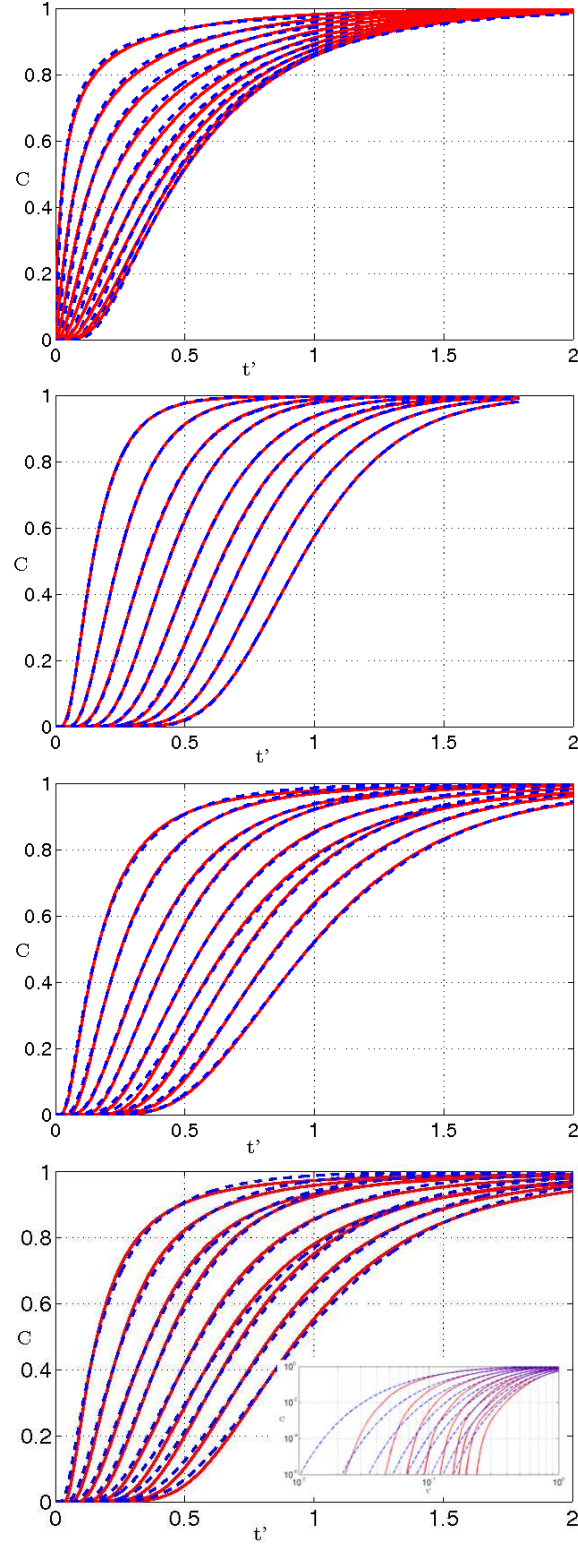
Figure 3.11: Comparison between breakthrough curves (normalized dimensionless solute concentration, continuous red line) over dimensionless time $t' = t\varepsilon/q$ obtained by surface-averaging over equidistant sections of the porous medium for different Péclet numbers (from top to bottom, Pe $= 1.9 \times 10^{-1}$, Pe $= 1.9 \times 10^1$, Pe $= 1.9 \times 10^3$, Pe $= 1.3 \times 10^5$) with the analytic solutions of the semi-infinite advection-diffusion equation with the fitted parameters (dashed blue line). For the largest Pe number an insert in log-log scale is included.

velocity is then given by:

$$U_{\text{eff}} = \left(\frac{\varepsilon \mathcal{L}_{\text{x}}}{M_1} \right), \tag{3.2}$$

whereas the dispersion coefficient is given by:

$$D = \frac{M_2}{2\mathcal{L}_{\text{x}}} \left(\frac{U_{\text{x}}}{\varepsilon} \right)^3. \tag{3.3}$$

This method in general performs better for the estimations of porosity (or equivalently the Darcy fluxes) and hydrodynamic dispersion in terms of computational time, accuracy and stability. Since the two methods resulted, however, in very similar (if not almost identical) results, only the parameters estimated with the method of moments will be shown and discussed.

It is moreover interesting to observe that the simulated breakthrough curves, reported in Fig. 3.11, compare well with the analytical solutions with the parameters estimated with the method of moments. However, some small differences are observed especially in the case of large Péclet numbers. To highlight these differences, of primary interest when it comes to anomalous diffusion, an insert in log-log scale has been added.

Figure 3.12 shows the estimation of the effective velocity (U_{x}) divided by the value of U_{x} computed from the averaging for the different Péclet numbers. As it can be seen, the effect of diffusive flux (see Eq. (2.20)) is important for low Péclet numbers when they can be order of magnitudes larger than the advective fluxes. When this effect is no more visible (i.e. for high Péclet numbers), the estimated velocity is always slightly lower than the theoretical one. This is clearly explained by Eq. (2.20) where the gradient of porosity appears as an additional convective flux (in our case in fact the porosity in the last sections used for the fitting is about 3% lower than the initial one).
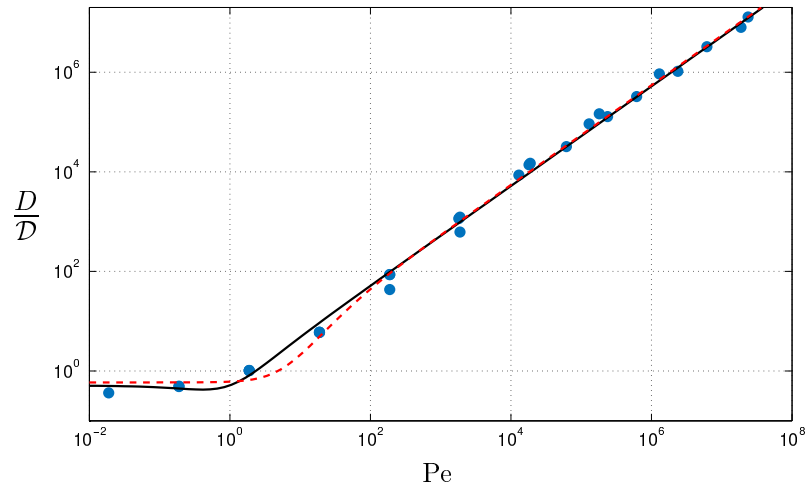
Figure 3.13 shows the estimated dispersion coefficients D divided by the molecular diffusion coefficient $\mathcal{D}$ for the different Péclet numbers investigated. It should be observed that the scaling of $D/\mathcal{D}$ with the Péclet number reproduces many recent computational results and classical power laws (obtained in turn by experimental and theoretical studies (Bear and Bachmat, 1967; Sahimi, 2012; Auriault and Adler, 1995)). As it is seen a constant behavior is observed in the first region (very low Pe), followed by a superlinear relationship (with an exponent of 1.2) in the central part, and a linear scaling at very high Pe in the last part.

It is interesting to notice that in the constant part (Pe $\rightarrow$ 0) of the plot,
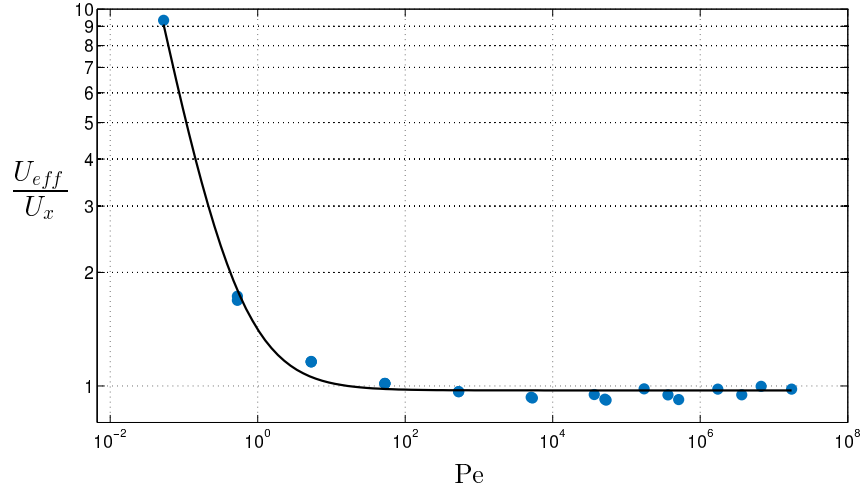
Figure 3.12: Effective transport velocity (blue circles), as estimated by the method of moments, and its fitting, of the form a + b/Pe (continuous line), with a = 0.97 and b = 0.15 .

Figure 3.13: Dispersion coefficients for different Péclet numbers, as estimated by the method of moments (blue circles) together with two fitted correlation laws; the continuous black line is Eq. (2.23) whereas the dashed red line is Eq. (2.24).

the result of Eq. (2.21), is confirmed. In fact, for this system the tortuosity was quantified to be about 1.2, resulting in a ratio between D and $\mathcal{D}$ of about 0.69 (as observable in Fig. 3.13). Considering the linear regime (high Péclet numbers) the already introduced expression: $D = \alpha V_x$, was found to be an adequate description for our medium; the constant α was estimated to be between 60 and 90 % of d_{50}, depending on the Péclet number.

Eventually, if the data of $D/\mathcal{D}$ versus Pe are fitted with the laws reported in Eqs. (2.23) and (2.24), the following results are obtained. The fitted parameters for Eq. (2.23) are: $\gamma = 0.51$, $\beta = 0.52$ and $\mathrm{Pe_c} = 0.99$, whereas for Eq. (2.24) are: $\gamma = 0.59$, $\alpha = 1.52 \times 10^{-4}$, and $\delta = 1.76$. It is interesting to highlight that the coefficient γ estimated with these two correlations are in good agreement with each other and with the estimation of tortuosity given by Eqs. (2.21) and (2.22). Both laws are reported (with these values of γ, α, β, δ and $\mathrm{Pe_c}$) in Fig. 3.13 together with our simulation results.

At last it is interesting to verify the validity of Fickian diffusion, that was used to close Eq. (2.19). In order to perform this analysis the quantity $\langle v'_x c' \rangle$, reported on the left-hand side of Eq. (2.19), was calculated and compared with the quantity reported on the right-hand side of Eq. (2.19) for ten different sections. This latter quantity is the product of the dispersion coefficient and the gradient on the main flow direction (x) of the surface-averaged concentration, $C(x)$, or in other words the dispersive flux as approximated by Fick's law, with the value of D_L calculated with the fitting performed with the method of moments. Typical results of this analysis for two superficial velocities are reported together with the dispersive fluxes at four different instants of the simulations in Fig. 3.14 and, as it is possible to see, the two curves are very close at low superficial velocity ($\mathrm{Re} = 9.6 \times 10^{-3}$). Larger deviations from the theoretical Fickian behavior are noticeable for higher velocities ($\mathrm{Re} = 66$), where vorticity and wakes develop more extensively. However, for both cases the hypothesis of Fickian behavior can be safely assumed.

3.3   Conclusions

Pore-scale simulations of single phase flows and scalar transport have been carried out by means of CFD with high-order numerical schemes and advanced meshing techniques. Wide ranges of Reynolds (from 10^{-4} to 10^2) and scalar Péclet (from 10^{-2} to 10^6) numbers have been investigated, including non-linear regimes. Results from steady-state (for flow field) and transient (for transport) simulations have been extracted on a hundred mesh slices perpendicular to the $x-$axis. Permeability, mean tortuosity, and mean shear
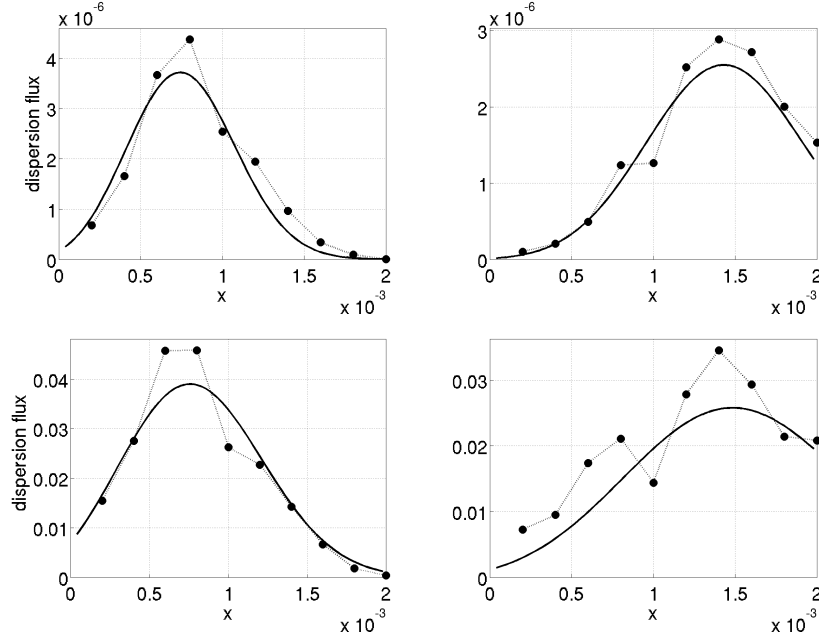
Figure 3.14: Comparison of the dispersion flux $\langle v'_x c' \rangle$ (m s^{-1}) along the flow x-coordinate (m) as calculated from the three-dimensional simulations (dotted lines with symbols) and as approximated by Fick's law (computed as the spatial derivative of the analytic solution for semi-infinite media with the fitted parameters, continuous line) for two different Reynolds numbers (top: Re $= 9.6 \times 10^{-3}$; bottom: Re $= 66$) and at two instants (from left to right).

rate have been calculated explicitly from the flow field results, while the dispersivity has been estimated with post-processing tools based on the method of moments and on the least square formulation of the inverse problem.

The results demonstrate the validity of the method, predicting the linear and non-linear regimes of Darcy's law with well-defined permeability and tortuosity constants in the first regime, and three different regimes for hydrodynamic dispersion (Sahimi, 1995): the first one is dominated by the molecular dispersion (for low velocity and fine particles), then a region where the mechanical and molecular dispersion are of the same order of magnitude, and finally a region where the dispersion depends linearly on the Péclet number, where the inertial effects dominate. This correlation for the hydrodynamic dispersion in terms of Péclet number is verified for the porous medium under study with the proposed simulation and upscaling tools. The asymptotic dispersion regime is quickly reached and dispersion is well approximated by the Fickian hypothesis, even if the fluid velocity distributions are not Gaussian. Further studies will include a more careful

characterization of the influence of the porous structures in terms of porosity and tortuosity and numerical upscaling of more complex macroscopic models will also be considered.